CdSe/CdS/CdTe Core/Barrier/Crown Nanoplatelets: Synthesis, Optoelectronic Properties and Multi-Photon Fluorescence Upconversion

Ali Hossain Khan,[1,2] Guillaume H. V. Bertrand,[2] Ayelet Teitelboim,[3] Chandra Sekhar M.,[1] Anatolii Polovitsyn,[2] Rosaria Brescia,[2] Josep Planelles,[4] Juan Ignacio Climente,[4,] Dan Oron,[3,*] and Iwan Moreels[1,2,*]*

[1] Department of Chemistry, Ghent University, Krijgslaan 281-S3, 9000 Ghent, Belgium.

[2] Istituto Italiano di Tecnologia, Via Morego 30, 16163 Genova, Italy.

[3] Department of Physics of Complex Systems, Weizmann Institute of Science, Rehovot 7610001, Israel.

[4] Departament de Química Física i Analítica, Universitat Jaume I, 12080 Castelló de la Plana, Spain.

Abstract

Colloidal 2D nanoplatelet heterostructures are particularly interesting as they combine strong confinement of excitons in 2D materials with a wide range of possible semiconductor junctions due to a template-free, solution-based growth. Here we present the synthesis of a ternary 2D architecture consisting of a core of CdSe, laterally encapsulated by a type-I barrier of CdS, and finally a type-II outer layer of CdTe as so-called crown. The CdS acts as a tunneling barrier between CdSe- and CdTe-localized hole states, and through strain at the CdS/CdTe interface, it can induce a shallow electron barrier for CdTe-localized electrons as well. Consequently, next to an extended fluorescence lifetime, the barrier also yields emission from CdSe and CdTe direct transitions. The core/barrier/crown configuration further enables two-photon fluorescence upconversion, and, due to a high nonlinear absorption cross section, even allows to upconvert three near-infrared photons into a single green photon. These results demonstrate the capability of 2D heterostructured nanoplatelets to combine weak and strong confinement regimes to engineer their opto-electronic properties.

Keywords nanoplatelets, ternary architecture, photoluminescence, *k·p* calculations, fluorescence upconversion

Combining semiconductors at the nanoscale offers the possibility to tune electron and hole wave functions and their corresponding overlap, by choosing materials with the appropriate valence and conduction band offset. In colloidal nanocrystals, such wave function engineering has already resulted in type-I (*e.g.* CdSe/ZnS)[1–3] and type-II (*e.g.* CdTe/CdSe) quantum dots (QDs),[4] as well as intermediate systems such as CdSe/CdS QDs[5–7] where, in a regime of strong quantum confinement, the small conduction band offset leads to an electron delocalization over the entire heterostructure, while the hole remains confined to the CdSe core region (referred to as a quasi-type-II band offset).[8] Type-I, type-II and quasi-type-II colloidal heteronanocrystals can be synthesized in a variety of shapes such as 0D dot-in-dot,[5] 1D rod-in-rod,[9] 2D core-crown nanocrystals,[10] or heterostructures with mixed dimensionality such as dot-in-rods[11] and dot-in-plates.[12] Heteronanocrystals offer a myriad of advantages, for instance a large absorption cross sections and sizeable Stokes shifts in giant-shell QDs, efficient nonlinear emission due to reduced Auger recombination rates in quasi-type-II QDs, or polarized absorption and emission properties in anisotropic QDs.[6,13]

Among the different colloidal nanostructures, 2D nanoplatelets (NPLs) take a specific position. They combine strong and weak quantum confinement regimes, which yields on the one hand a band-edge emission peak at discrete wavelengths,[14–16] and on the other hand a large band-edge oscillator strength and fast emission lifetime that scales with the area of the NPL.[17] The thickness can be controlled with monolayer precision, resulting in narrow emission line widths that are homogeneously broadened at room temperature.[16] Due to the large NPL volume enabling weakly confined 2D excitons, they also exhibit a high two-photon absorption coefficient,[18] and the 2D shape leads to opportunities for self-assembly and ultrafast Förster energy transfer between NPLs.[19]

Recently, a variety of Cd-based NPL heterostructures have been synthesized, which can further shape the electron and hole wave functions.[20–24] In the case of concentric hetero-NPLs, type-I CdSe/ZnS NPLs yield fast photoluminescence (PL) lifetime,[25] in combination with a red shift of the band edge, while quasi-type-II CdSe/CdS core/shell NPLs combine an even larger red shifted emission with a reduced PL decay rate.[26] One can also laterally extend the NPLs by growing a second material around the NPL edges. Interestingly, in this so-called core/crown configuration, the CdSe/CdS conduction band offset of *ca.* 300 meV is sufficient to retain the exciton confined to the core, yielding a type-I heterostructure,[10,26,27] highlighting the benefits of combining weak with strong confinement in 2D hetero NPLs. Type-II core/crown heterostructures, finally, have been also been produced, in the form of in CdSe/CdTe or CdS/ZnSe NPLs,[28–30] as well as alloyed crown and multi-crown (CdSe/$CdSe_{1-x}Te_x$, CdSe/$CdSe_{1-x}Te_x$/CdS) heterostructured NPLs .[30–33]

Considering the elements above, we created an even more elaborate ternary heterostructure, that allows to further engineer emission properties and carrier dynamics in 2D nanoplatelets. In this manuscript, we present the insertion of a type-I barrier in the CdSe/CdTe type-II junction, through synthesis of CdSe/CdS/CdTe core/barrier/crown NPLs. Ternary architectures are known to increase the lifetime of charge-separated excitons or are engineered to control excited-state carrier dynamics,[34] and have been developed as efficient dual-emitters.[34–36] In addition, they make excellent up-conversion phosphors by creating hole- or electron-specific tunneling barriers. Our ternary architecture was chosen due to its potentially interesting band alignment, with a cascaded conduction band alignment permitting electron relaxation into the CdSe region, while the holes remain confined to either CdSe or CdTe due to the CdS valence band barrier. As a result, next to the extended exciton lifetime due to the charge-separated exciton, we also obtained two-photon

and even three-photon upconversion fluorescence, the latter mediated by the efficient nonlinear absorption coefficient enabled in 2D NPLs as discussed by Scott *et al*.[18]

Result and Discussion

Based on our previous work, we first synthesized 4.5 monolayer (ML) thick CdSe NPLs with controlled thickness and aspect ratio.[37] A typical sample is shown in **Figure 1a**, and has lateral dimensions of 36 nm by 4.2 nm. Following Dubertret *et al.*,[10,28] we synthesized CdSe/CdS and CdSe/CdTe core/crown 2D NPLs as a reference for our CdSe/CdS/CdTe core/barrier/crown (CBC) NPLs. CdSe/CdS NPLs show the typical features of a type-I heterostructure, with the absence of a red shift of the emission peak after crown growth, and a fast, monoexponential PL decay with a 3.3 ns lifetime (SI, **Figure S1**). CdSe/CdTe NPLs on the other hand display a strong band-edge red shift, with a PL emission at 637 nm and an extended PL lifetime of 124 ns (SI, **Figure S2**), representative for type-II heterostructures. Based on these syntheses, we adopted a multi-step, one-pot approach to create both CdS barrier and final CdTe crown. CdS and CdTe growth solutions were added consecutively, without intermediate isolation and purification of the CdSe/CdS NPLs. The 4.5 ML CdSe core NPLs were dispersed in 1-octadecene (ODE) along with cadmium propionate ($Cd(Prop)_2$). After degassing at 110°C, the reaction temperature was increased to 235°C and the CdS growth solution (containing sulfur dissolved in ODE, oleic acid and cadmium acetate dihydrate, $Cd(OAc)_2.2H_2O$) was added dropwise for 2 min using a syringe pump, at a rate of 3 mL per hour. After the injection of the CdS growth solution, the reaction was stirred for another 5 min at 235°C. An aliquot was collected at that point to verify the CdS barrier thickness and to compare with the final CBC NPLs. As the CdS growth was executed under high cadmium excess (Cd:S ratio of 112:1), we only added additional Te

(trioctylphosphine telluride dissolved in ODE) in the second step, again dropwise over the course of 3 min at a rate of 3 mL per hour, followed by stirring for another 5 min. In **Figure 1**, we show transmission electron microscopy (TEM) images, depicting the result of a typical reaction, where we obtained CdSe/CdS NPLs with dimensions of 37 nm by 5.5 nm (**Figure 1b**) and finally, after CdTe crown growth, CBC NPLs of 52 nm by 9.1 nm (**Figure 1c**). A scheme depicting the synthesis route is shown in **Figure 1d**.

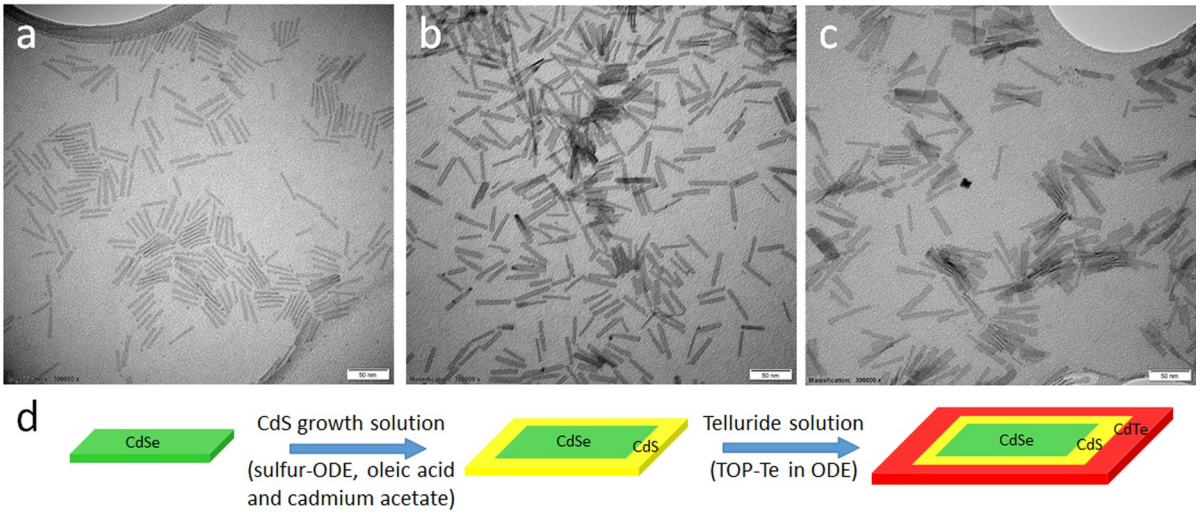

Figure 1. TEM images of (a) CdSe core, (b) CdSe/CdS core/barrier and (c) CdSe/CdS/CdTe core/barrier/crown NPLs (scale bars: 50 nm). (d) Schematic representation of the synthesis of core/barrier/crown NPLs.

The CBC NPLs show the typical absorption features at 508 nm and 567 nm for the band-edge transitions of CdSe core and CdTe crown respectively (**Figure 2a**), while a CdS absorption onset can be discerned around 400 nm. The spectral position of the absorption peaks confirms that the 4.5 ML thickness does not change when growing the CdS and CdTe crown.[14] As the heavy hole-electron transition for a 4.5 ML CdTe NPLs was expected around 554 nm (SI, **Figure S2a)**,[14] the red shifted value may be due to some inclusion of sulfur into the CdTe crown.[38,39] In the fluorescence spectrum, we measured three emission peaks (**Figure 2b**), two spectrally narrow signals at 510 nm and 575 nm, and a broad band at 625 nm. These can be associated with the

CdSe band-edge, the CdTe band-edge and the indirect exciton transition, respectively, which are typically quenched in CdSe/CdTe NPLs (SI, **Figure S3**).[28,30] Indeed, while in our CdSe/CdTe reference sample no more than 0.001% of the total spectrum consists of CdSe band-edge emission (SI, **Figure S3**), in the sample shown in **Figure 2**, about 5% of the total area under the emission spectrum can be assigned to the combined CdSe and CdTe band-edge emission peaks (SI, **Figure S4**). The indirect character of the emission at 625 nm is revealed by the extension of the PL decay time to 182 ns (**Figure 2c**). The lifetime of the direct transitions (from CdSe and CdTe) of CBC NPLs was also measured, and compared with core-only and core/barrier NPLs (SI, **Figure S5**). The PL decay curve was fitted with a tri-exponential function, from which the amplitude-weighted average life time was calculated. The average lifetime of the CdSe emission decreases from the core-only to the CdSe/CdS NPLs, and the value of 3.9 ns is similar to our CdSe/CdS reference sample (SI, **Figure S1**). The CdSe PL lifetime is even slightly shorter in CBC NPLs, which we attribute to Förster resonance energy transfer from the CdSe core to the CdTe crown. The lifetime of the emission at 575 nm of CBC NPLs equals 76 ns, however, as the CdTe emission is weak and superposed on the type-II emission, we cannot disentangle both contributions.

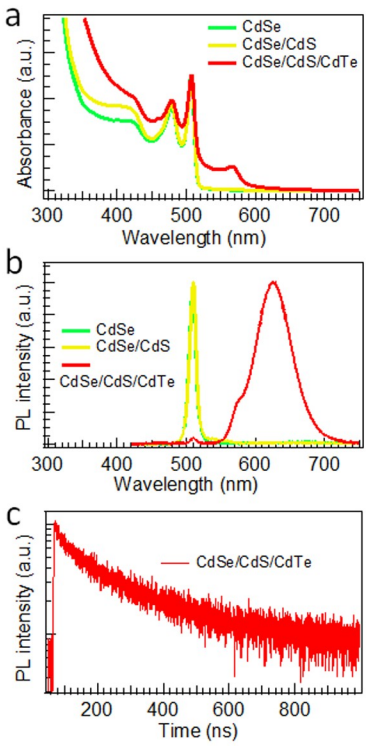

Figure 2. (a) Absorbance and (b) PL spectra of CdSe, CdSe/CdS and CdSe/CdS/CdTe NPLs, respectively. (c) PL decay trace of the type-II transition monitored at 625 nm.

PL excitation (PLE) spectroscopy supports that the emission peaks originate from a single heterostructure. First, when monitoring the emission at 510 nm for CdSe core-only, CdSe/CdS core/barrier and CdSe/CdS/CdTe CBC NPLs, we observed that this emission peak can be excited *via* the CdSe absorption, and by comparing core-only CdSe with CdSe/CdS and CdSe/CdS/CdTe, a small increase from 420 nm onward indicates that the CdSe emission can be excited *via* the CdS absorption as well (**Figure 3a**). Second, the emission associated with the indirect transition in CBC NPLs, which we monitored at 625 nm, can be excited *via* the same absorption features that lead to the 510 nm CdSe band-edge emission in those heterostructures, as well as the CdTe absorption, confirming that we indeed probe a single heterostructure (**Figure 3b**). We have also used another sample of CBC NPLs (Batch5) with more prominent CdS

absorption (*i.e.* a wider CdS barrier) and performed the PLE measurements as mentioned above (**Figure S6**). Here we more clearly observed the CdS absorption for all the PLE spectra, in addition to the CdSe and CdTe features, again supporting the CBC structure.

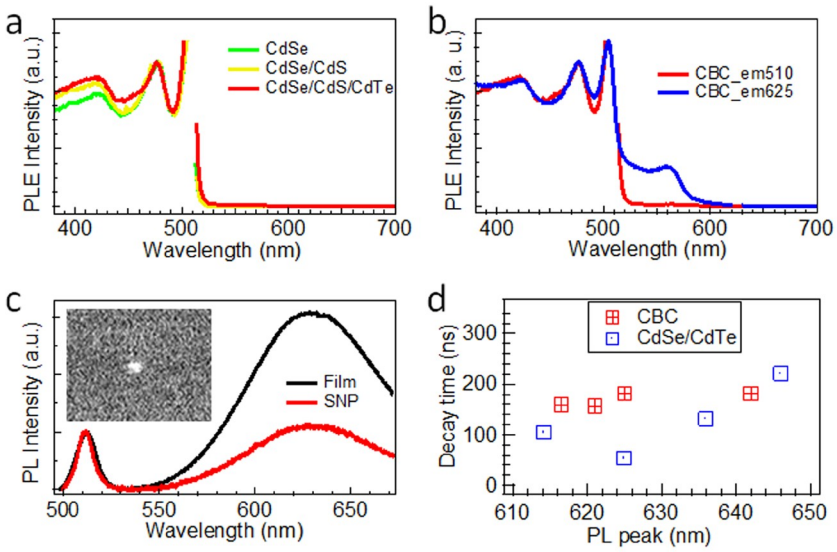

Figure 3. (a) PLE spectra, monitored at the CdSe emission at 510 nm for CdSe, CdSe/CdS and CdSe/CdS/CdTe NPLs. (b) PLE spectra of the CdSe/CdS/CdTe CBC NPLs monitored at 510 nm and at the 625 nm indirect transition. (c) PL spectra of a CBC NPL thin film and of a single CBC NPL at room temperature (Batch5). Inset: Micrograph of the single CBC NPL. (d) Plot of the PL decay times against PL peak positions of the CBC samples (red squares) compared with the CdSe/CdTe reference samples (blue squares).

To further confirm the ternary heterostructures we have performed high-angle annular dark-field scanning TEM energy dispersive X-ray spectroscopy (HAADF STEM-EDS). However, while we clearly observed the Se, S, and Te signals in the EDS maps, we also noticed a significant electron-beam-induced degradation of the CBC NPLs (SI, **Figure S7**), hindering a clear mapping on a single-particle level. We therefore resorted to single-NPL optical spectroscopy. **Figure 3c** shows a comparison of the PL spectrum of a single CBC NPL (SNP) with the corresponding close-packed thin film. Both the direct CdSe transition and the type-II emission of the CBC NPLs are clearly observed on a single NPL, with a decrease in full-width-at-half-maximum for

the CdSe emission, from 13.6 nm in the thin film to about 10-11 nm for different single NPLs (SI, **Figure S8**, **Table S1**). A single-particle micrograph of CBC is shown in the inset of **Figure 3c**. Note that we did not discern the CdTe emission in this sample (**Figure 3a**, SI, **Figure S6**), however, this is explained by the relatively small CdTe crown (SI, **Table S2**). Overall, about 2 in 10 NPLs did only show the type-II emission, indicative of NPLs with an incomplete CdS barrier, and a minor fraction (2 out of 50 NPLs) only showed the CdSe emission, suggest that they contain no CdTe crown. We did not observe particles that either show emission at other emission wavelengths that the ones above, or at the wavelength of the CdTe NPL band-edge emission, leading to the conclusion that the synthesis does not lead to co-nucleation of separate nanocrystals, and that the CdTe emission observed in the ensemble PL spectrum should also pertain to the CBC NPLs, as also demonstrated by the PL excitation spectroscopy.

Controlling the barrier and crown dimensions was achieved by injecting different amounts of Cd/S and Te growth solutions, always maintaining a fixed injection rate of 3 mL per hour (**Table S2** and **Figure S9**). In all cases the reaction solution was stirred for 5 min before the injection of the Te solution. The resulting PL peak position of the type-II transition can be varied between 617 nm and 642 nm, similar to CdSe/CdTe NPLs without a CdS barrier (**Figure S10**). A measurement of the PL decay of the indirect transition in the different samples (**Figure S10c**) shows first that the PL decay time in CdSe/CdTe is dependent on the crown size. However, independent of these results, inclusion of a CdS barrier leads to an increased PL lifetime (**Figure 3d** and SI, **Table S3**) when compared to CdSe/CdTe core/crown NPLs that emit at a similar wavelength. Note, for both CBC and CdSe/CdTe NPLs we started from a CdSe core with similar dimensions. The data above are in line with the presence of a type-I CdS barrier for the hole, inserted between the CdSe core and the CdTe crown, leading to a reduced electron-hole overlap.

Hence, taking the transmission electron microscopy, which showed that we grow larger structures upon addition of CdS and then CdTe, the comparison between ensemble and single-particle PL spectra, which confirmed that CdSe and broad peaks are reproduced on a single-particle level, PL excitation spectra, which demonstrate that the CdTe emission can be excitated *via* the CdSe absorption, and the spectral and temporal tunability of the broad emission with crown dimensions, we can conclude that we synthesized CBC ternary heterostructured NPLs, which exhibit both direct CdSe and CdTe emission, and as well and an indirect emission peak.

The general band structure, derived from bulk band offsets and depicted in **Figure 4a** and **Figure 4b** shows how CdSe emission can be obtained when exciting the CdSe core directly, or when carriers relax in this region *via* excitation of the CdS barrier. To explain the CdTe emission however, one needs to invoke a barrier for electron relaxation as well. This barrier may be caused by strain at the CdS/CdTe interface or be induced directly by the electron-hole Coulomb interactions, and was investigated in further detail with $k \cdot p$ calculations. To this purpose, different CBC heterostructures were considered. We started by calculating the band structure of a CBC NPL with a narrow CdS barrier, comparable to experimental sample Batch3 (**Figure 4c)**, and a CBC NPL with a wide CdS barrier, comparable to sample Batch4 (**Figure 4d)**. The narrow-barrier NPL has a CdSe core of 25 nm by 5 nm, a CdS barrier of 1 nm by 1 nm, and a CdTe crown of 15 nm by 5 nm. The wide-barrier NPL has the same core and CdTe crown dimensions, but the CdS barrier is 15 nm by 5 nm. Both NPLs have a 4.5 ML thickness, assuming the CdSe lattice constant prior to strain relaxation. Electron and hole states are calculated with single-band $k \cdot p$ Hamiltonians, including dielectric mismatch with the organic medium and strain in the continuum elastic approximation (see SI for details on the calculation).

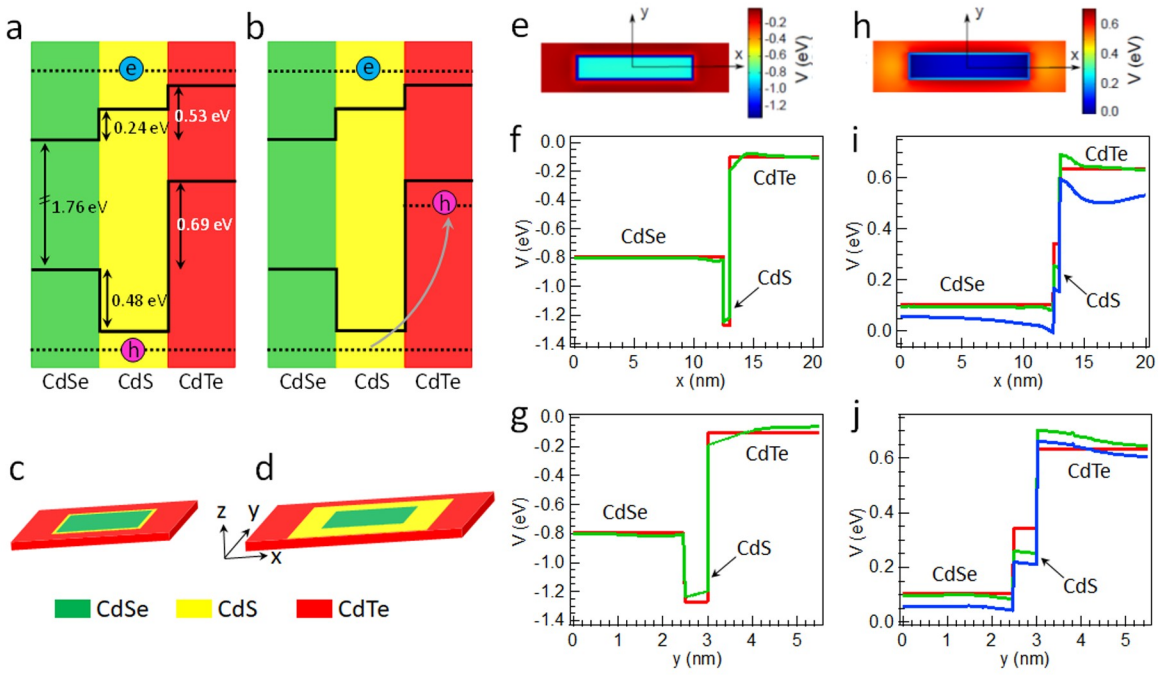

Figure 4. (a-b): Conduction and valence band alignment in the CBC heterostructure, considering unstrained band offsets. (a) A hot electron-hole pair is created. (b) The hole relaxes faster than the electron, conditioning the potential landscape that the hot electron sees at the moment of relaxation. (c-d) Schematic of the CBC NPLs under study, resembling Batch3 with a narrow CdS barrier (c), and Batch4 with a wider barrier (d). (e-g) Potential landscape seen by a photo-excited valence band hole for a narrow-barrier sample, with a 2D in-plane cross section (e), and 1D profiles along *x*- (f) and *y*- semi-axes (g), as depicted in (e). In the 1D plots, red and green lines show the potential excluding and including the influence of strain. The origin of energies is taken at the top of the CdTe band. (h-j) Same as (e-g), but for conduction band electrons. Blue lines in (i) and (j) panels show the potential including the Coulomb attraction exerted by the hole ground state localized in the CdTe crown. The origin of energies is taken at the bottom of the CdSe band.

As we are interested in determining the origin of the CdTe emission, calculations are based on the consideration that the hot electron-hole pair relaxes as shown in **Figure 4**. Initially, the hot electron and hot hole have high energy and barely feel the band offset profiles (**Figure 4a**). The hole relaxes faster than the electron, because the larger band offset and heavier mass (SI, **Table S4**) provide a higher density of states, favoring phonon-mediated decay. This implies that the hot electron likely sees the Coulomb potential generated by the hole that has already relaxed to the

CdTe crown band edge. The resulting potential landscape seen by valence band holes is shown in **Figure 4f** and **Figure 4g**. The self-energy repulsion due to dielectric mismatch, V_{self}, shifts down the potential energy about 100 meV for all three materials, but it does not affect the relative band alignment. The main term affecting the band alignment is the unstrained band offset, V_{bo}, which turns CdS into a 0.48 eV high valence band barrier between the CdSe core and the CdTe crown (red line). Strain (SI, **Figure S11**) somewhat modifies the overall potential (green line, and SI, **Figure S12** for calculations on the CBC NPL with wide CdS barrier), yet in any case, it yields only minor modifications as compared to V_{bo}.

Figure 4i and **Figure 4j** show the potential landscape seen by the electrons. In this case we have a cascaded band alignment, again mainly set by V_{bo} (red lines in 1D plots). Here strain does play a role. It raises (lowers) the potential in the CdSe (CdS) region, thus reducing the CdSe-CdS barrier from ~0.25 eV to ~0.20 eV. In addition, strain on the CdS/CdTe interface gives rise to a narrow potential well (barrier) on the CdS (CdTe) side (green line). In principle, this feature is capable of inducing localized states on the CdS barrier and/or confined states in the CdTe crown, which will now see a barrier up to 60 meV for narrow CdS and up to 80 meV for wide CdS. The inclusion of the Coulomb interaction with the hole ground state, localized in the CdTe crown, further enhances the depth of the barrier at the CdS/CdTe interface (**Figure 4i** and **4j**, blue line), up to 90 meV for narrow CdS and up to 110 meV for wide CdS. The features are again shared qualitatively by wide and narrow barrier NPLs (SI, **Figure S12**), although the effect is quantitatively stronger on the wide ones, because the CdTe side of the interface is slightly more compressed by strain (SI, **Figure S11**).

These calculations already reveal that band bending due to strain and Coulomb interactions, which leads to local potential wells, can capture charges in a ground- or high-energy state, with a

wave function that can localize in either in CdSe core or CdTe crown (see SI, section on *k·p* calculations for electron and hole wave function localization as a function of energy), they do not yet yield direct insight in the possibility for CdTe or CdSe band-edge emission. To this end, we also evaluated if the CdS barrier can influence the nonradiative decay of photo-excited electron-hole pairs, and yield metastable states which can recombine radiatively in CdTe and CdSe before forming the indirect exciton. We assumed that the nonradiative decay is driven by phonons. The carrier-phonon coupling Hamiltonian, and hence the ensuing decay rate, is related to the inter-level energy spacing –which determines the density of available acoustic or optical phonon modes– and the carrier-phonon matrix element.[40] **Figure 5** shows that the inter-level energy spacing is similar in both cases studied (narrow and wide barrier), therefore, we focused on the carrier-phonon matrix element. Within the dipolar approximation, the element is proportional to ¿⟨*f*|$\vec{r}$|*i*⟩∨¿, where *i* and *f* are the initial and final electron or hole states. Hence the relaxation is determined by the wave function overlap between initial and final states.

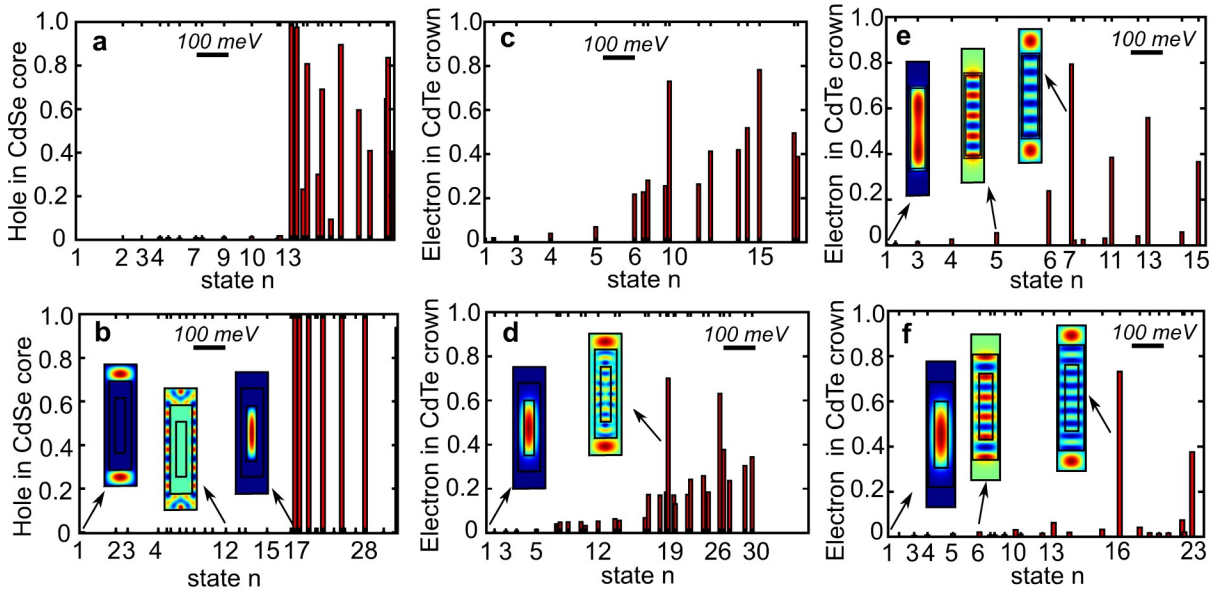

Figure 5. (a-b): Normalized fraction of the hole density that is localized in the CdSe core for different states with A_g symmetry, $|A_g, n\rangle$, for narrow- (a) and wide-barrier (b) NPLs. A 100 meV scale bar is included in the figures to illustrate the energy scale. The insets show a few

representative envelope wave functions. The states are almost completely localized either in the CdTe crown or in the CdSe core. (c-d): Same plot for the density of electrons localized in the CdTe crown. Low-energy states remain confined to the CdSe core, while high energy states delocalize over the entire NPL. (e-f) Normalized fraction of the electron density localized in the CdTe crown for different states, in a NPL with narrow (e) and wide (f) CdS barrier, and a CdTe crown of 15 nm × 1 nm (narrow along the *y*-direction). The insets show a few envelope wave functions. In (f), the *n = 16* state shows strong localization in CdTe, while all other states at lower energy are almost completely localized in CdSe and CdS.

Figure 5, panels (a) and (b) represent the fraction of the hole charge density localized inside the CdSe core for narrow and wide barrier NPLs, respectively. We consider holes with A_g symmetry (within the D_{2h} group), $|A_g, n\rangle$, although the same observations hold for different symmetries. As expected, hole states localize either in the CdTe crown (with a nearly zero CdSe core density) or in the CdSe core (CdSe core density nearly one). Low-energy states mostly localize in the crown, while high-energy states can be either in the crown or in the core. Very little charge density is localized in the CdS barrier, and we found no states within the energetic window that we consider (up to 0.8 eV above the ground state) that are delocalized over both core and crown. This is a consequence of the high and relatively wide type-I CdS barrier. Using a narrow barrier (**Figure 5a**), this effect is reduced, however, lowest-lying states still have an either CdSe-core or CdTe-crown localization, justifying a long-lived metastable hole state for the CdSe core.

Panels (c) and (d) of **Figure 5** show the electron density in the CdTe crown. Because CdSe offers the lowest potential, low energy states are mostly localized in the core and barrier (CdTe crown charge densities are nearly zero), but here the localization in the crown increases gradually with state energy. A few states appear with dominant (over 70%) charge density in the crown, in spite of CdTe having high energy (**Figure 4h-4j**). Such states partly arise from the small strain barrier on the CdS/CdTe interface. Nevertheless, the barrier is quite shallow and, unlike in the case of

holes, one finds electron states with partial localization in both CdSe core and CdTe crown even for a wide CdS barrier, and no long-lived electron state is derived.

However, in accordance with the experimental dimensions of the CBC NPLs, an important geometrical consideration still has to be considered: the presence a CdTe crown with limited width (SI, **Table S2**, Batch2). To this end, we calculated electron states for the CBC NPLs with crown with that is reduced from 5 nm to 1 nm. The resulting electron density is plotted in **Figure 5e-5f**. Interestingly, for a wide CdS barrier, the *n = 16* state arises as an isolated state with large (almost 80%) localization in the CdTe crown, while neighboring states and lower-lying states have densities well below 10%. When compared to the wide crown (**Figure 5d**), where neighboring states reached densities of 20%, one notices that the narrow crown translates into a better separation of states localized in the core and states localized in the crown. These results are consistent with experimental data, where Batch2 NPLs for instance show a distinct emission from the CdTe crown with a relative weight of 6.7% (SI, **Figure S9**). The role of the CdTe crown width can be interpreted as follows. Because the NPLs have in-plane anisotropy, electron states are more sensitive to the confinement in the narrow direction (width) than to that in the long direction (length). When growing wide CdTe crowns, electron states -even if low in energy- are prone to deposit part of their charge in the CdTe crown to minimize confinement energy. If the crown is narrow, this is no longer possible and states with more definite localization (in CdSe core or in CdTe crown) are enabled.

Associated relaxation rates derived from ¿$\langle f|\vec{r}|i\rangle$∨¿ are discussed in the supporting information (SI, **Figure S13**), and support our conclusions. For valence band holes, the large (bulk) band-offsets turns CdS into a high potential barrier, leading to hole states which are localized either in the CdSe core or in the CdTe crown. This implies excited hole states localized in CdSe have

slow phonon-mediated recombination rates towards the CdTe crown, and explains the CdSe emission observed. For conduction band electrons, a moderate potential barrier forms at the CdS/ CdTe interface, producing excited electron states that are largely (for 70-80%) localized in the CdTe crown. Electron localization either in CdSe or in CdTe is further favored by the presence of a narrow CdTe crown. Altogether, calculations yield metastable electron states mainly localized in CdTe, with relatively slow phonon decay rates towards CdSe, which are consistent with the CdTe emission observed.

Clearly, experimental data and *k·p* calculations support the formation of CdSe/CdS/CdTe CBC heterostructures with distinct type-II as well as CdSe and CdTe band-edge emission features. The ternary heterostructure combines an indirect ground state with direct excited-state transitions, and should therefore allow for fluorescence upconversion. As reported previously, colloidal nanocrystals are particularly well suited for fluorescence upconversion,[41–43] in particular CdSe:Te/CdS/CdSe,[44] PbSe/CdSe/CdS[45] and PbS/CdS-CdSe/ZnS[46] QDs have already demonstrated relatively high upconversion efficiencies (of the order of several percent) of near infrared light. Here we excited sample Batch2 with 5 ns pulses at a repetition rate of 10 Hz, probing the CBC NPL transient fluorescence spectrum to investigate the upconversion process. Excitation wavelengths were selected in order to distinguish between linear and nonlinear excitation (**Figure 6**). For CBC NPLs, 460 nm is energetic enough to directly excite the CdSe region, and obtain CdSe band-edge fluorescence in the single-photon regime. In contrast, using a pump wavelength of 580 nm or 640 nm, we can excite only the CdTe or the indirect transition, respectively, which requires two photons for detection of the excited-state CdSe emission. The transient decays at 515 nm and 620 nm, corresponding to the CdSe band edge and the indirect transition respectively, are well fitted with a biexponential function (**Figure 6f**), with lifetimes of

$\tau_1^{515}=8.4\,ns, \tau_2^{515}=100$ ns and $\tau_1^{620}=78\,ns, \tau_2^{620}=390$ ns, corroborating our time-resolved PL decay measurements.

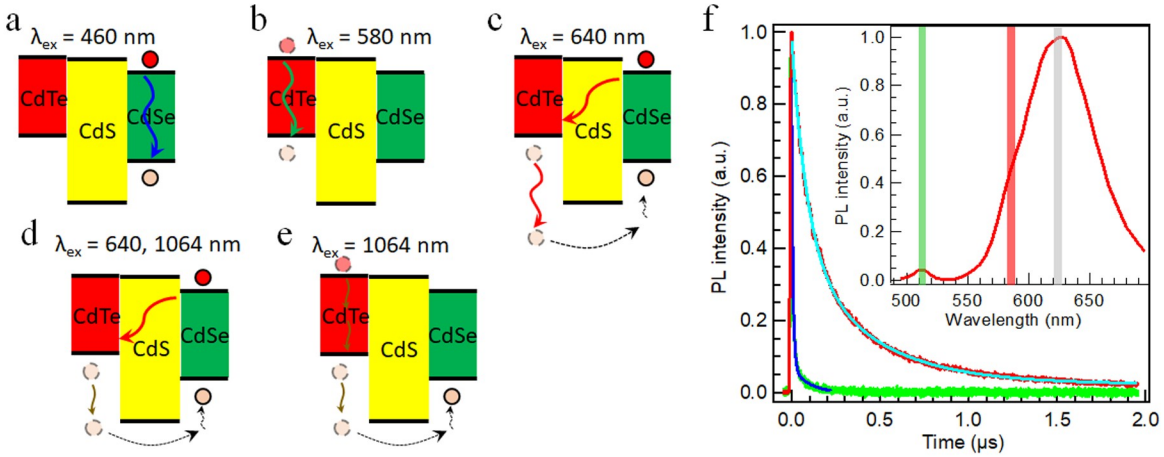

Figure 6. NPL band alignment and photo-excitation schemes. (a) Linear excitation of the CdSe core at $_{ex}$ = 460 nm (exciting the CdTe crown and the indirect transition as well). (b) Linear excitation of the CdTe crown (and the indirect transition) using $_{ex}$ = 580 nm. (c) Two-photon upconversion excitation of the CdSe core *via* the indirect transition, using $_{ex}$ = 640 nm. (d) Pump-probe two-photon upconversion excitation of the CdSe core using a 640 nm excitation combined with a 1064 nm intraband absorption. (e) Three-photon upconversion excitation of the CdSe core, using two 1064 nm photons to excite the CdTe crown *via* two-photon absorption, followed by a 1064 nm intraband excitation. (f) NPL fluorescence decay ($_{ex}$ = 460 nm, fluency 53 μJ/cm^2) for the CdSe band-edge emission at 515 nm (green trace) and the indirect transition at 620 nm (red trace). The spectrum depicted in the inset is calculated from the time-integrated emission decay. The band-edge emission for the different transitions (CdSe, CdTe peak and the indirect transition,) with the respective collection wavelength are marked in green, red and grey respectively.

First, a power series for different excitation wavelengths was acquired to check for the dependence of fluorescence intensity on excitation fluency and ensure that we excite the CBC NPLs below the saturation regime (SI, **Figure S14**). Second, by exciting the sample with two 640 nm photons, we observed upconverted fluorescence at 515 nm arising from the CdSe core (**Figure 7**). The excitation proceeds through the formation of an indirect transition exciton,

followed by either Auger recombination or intraband absorption to excite the hole into the CdSe region. The process was well fitted with a simplified Poisson distribution for the probability to absorb photon pairs:

$$FL_{UC} = \left(\frac{I^2}{2!} + 2 \cdot \frac{I^3}{3!} + 3 \cdot \frac{I^4}{4!} + 4 \cdot \frac{I^5}{5!} + 5 \cdot \frac{I^6}{6!} + \ldots \right) \cdot e^{-I} \cdot \epsilon_{UC} \quad , \quad I = \frac{I_{ex}}{I_{sat,UC}}$$

FL_{UC} equals the upconverted fluorescence intensity, and $\epsilon_{UC} < 1$ is the upconversion efficiency, *i.e.* the probability to heat up a hole and for it to be captured in the CdSe region before cooling. The saturation intensity was obtained as $I^{ex_{640}}_{sat,UC\,510} = 181\, mJ/cm^2$, and confirmed that we observed the upconverted fluorescence well below the saturation regime.

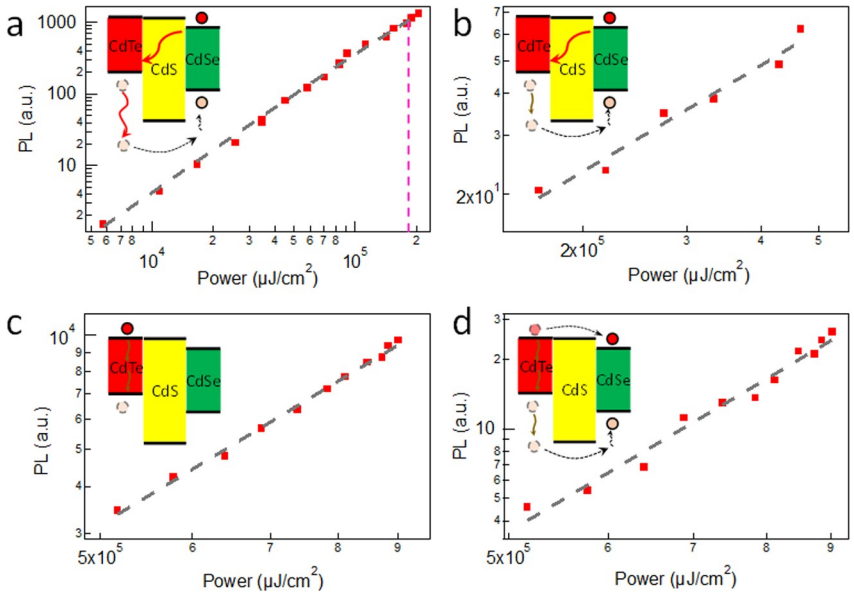

Figure 7. NPL fluorescence upconversion. (a) 640 nm upconversion excitation of the CdSe core. The data was fitted by a simplified Poisson distribution for the probability to absorb photon pairs plotted as the black dashed line. (b) Pump-probe upconversion excitation of the CdSe core using a 640 nm excitation with fixed excitation power, combined with a second pump at 1064 nm (yielding intraband absorption) with variable power. A fit of the power dependence $a \cdot P_{ex}{}^{b}$, with b = 1 is plotted as dashed line. (c) Two-photon excitation of the CdTe crown using 1064 nm excitation, monitored at 620 nm. A fit yields a b = 1.9 power dependence. (d) Fluorescence upconversion, monitored at 510 nm, created by three-photon excitation using $_{ex}$ = 1064 nm. A fit of the power dependence yields b = 3.3.

Using a second excitation photon at 640 nm implies that we cannot distinguish between hot hole creation *via* Auger recombination of two indirect excitons, or *via* intraband absorption. We therefore employed a pump-probe excitation scheme (**Figure 6d**), which comprised of an initial 640 nm excitation of the CBC NPLs at fixed excitation power (one fifth of the saturation power), combined with a second excitation at 1064 nm, that can only lead to heating of the CdTe valence band hole *via* intraband absorption. **Figure 7b** shows that the emission intensity at 510 nm, using the 640 nm – 1064 nm excitation scheme, fits a linear power dependence $a \cdot P_{ex}{}^{b}$ with b = 1, confirming that fluorescence upconversion occurs here *via* intraband absorption of the hole into a higher energy state and relaxation into the CdSe core.

In order to assess the upconversion efficiency ϵ_{UC}, a comparison can be made between the number of fluorescence counts per absorbed photon, at saturation intensity for two-photon ($I_{sat,UC513}^{ex_{640}}$¿ and linear excitation ($I_{sat,lin513}^{ex_{460}}$¿:

$$\epsilon_{UC} = \frac{FL_{sat,UC513}^{ex_{640}}}{FL_{sat,lin513}^{ex_{460}}} \frac{I_{sat,lin513}^{ex_{460}} OD_{460}}{I_{sat,UC513}^{ex_{640}} OD_{640}}$$

As both the upconversion ($FL_{sat,UC513}^{ex_{640}}$¿and the linear ($FL_{sat,lin513}^{ex_{460}}$¿fluorescence counts were measured at the same NPL concentration, the relation above yields the probability to excite the CdSe region, *i.e.* the efficiency of the upconversion process. It gives a ratio of 0.014:1, which means that 36 absorbed NIR photon pairs are equivalent to one absorbed visible photon. Compared to other colloidal nanocrystals,[44–46] this efficiency is quite modest, likely due to the relatively large crown area of 71 nm^2 (compared to the overall NPL area of 338 nm^2), and a possible remedy could be to further engineer the band structure to optimize relaxation of the hot hole toward the CdSe core.[46] On the other hand, the 2D shape offers a specific benefit. Due to the

high nonlinear absorption coefficient,[18] not only two-photon, but also three-photon upconversion is feasible. This was demonstrated by measuring the fluorescence upconversion using a 1064 nm excitation wavelength. As a result of two-photon absorption in the CdTe crown region around 532 nm, we first observed emission for the indirect transition at 620 nm, with a quadratic dependence on excitation fluency (**Figure 7c**, fitted power dependence with slope 1.9). Then, following intraband absorption through a third 1064 nm excitation photon, we then again obtained the CdSe core emission at 510 nm, here with a cubic fluency dependence (**Figure 7d**, fitted power dependence with slope 3.3).

Conclusion

We demonstrated the synthesis of a CdSe/CdS/CdTe 2D ternary heterostructure with an intermediate CdS barrier that separates emissive CdSe core and CdTe crown regions. This design allowed us to tune the indirect and direct transition energies and intensities as a function of the barrier and crown thickness. The theoretical results support the experimental data and reveal the formation of CdSe/CdS/CdTe core/barrier/crown nanoplatelets with distinct indirect as well as direct CdSe and CdTe band-edge transitions. While strong confinement applies to the vertical direction, 2D nanoplatelet charge carriers are typically only weakly confined in the lateral directions, which allowed us to obtain a type-I band offset at the CdSe/CdS interface, reducing the electron delocalization into the barrier and final CdTe crown. We obtained a heterostructure that exhibits efficient two-photon, and by the large nonlinear absorption coefficient induced by the 2D shape, even three-photon fluorescence upconversion. Our results demonstrate that shape-controlled colloidal nanocrystals offer an interesting pathway toward upconverting nanoparticles

that can transform near-infrared to visible light, with potential applications in near-infrared upconversion-based photodetectors, solar cells, or biomedical imaging.[47–49]

Experimental Methods

Chemicals. Cadmium nitrate tetrahydrate (99.997%), sodium myristate (99%), cadmium(II) acetate ($Cd(OAc)_2$; 99.995%), cadmium acetate dihydrate ($Cd(OAc)_2 \cdot 2H2O$), octadecene (ODE; 90%), oleic acid (90%), trioctylphosphine (TOP; 90%), propionic acid (99.5%) methanol (99.9%), hexane (95%) were purchased from Sigma-Aldrich. Cadmium oxide (99.999%) sulfur (S; 99.9%), selenium powder (Se; 99.99%) and tellurium (Te; 99.99%) were purchased from Strem Chemicals.

Synthesis of type-I CdSe/CdS core/crown NPLs. Cadmium myristate ($Cd(Myr)_2$) and CdSe NPLs were synthesized according to a published procedure.[37] A 0.1M solution of ODE-S in ODE was prepared by heating 32 mg of elemental sulfur in 10 mL of ODE. The CdS growth solution was prepared by mixing 2 mL of the 0.1 M ODE.S solution, 3 mL of ODE, 350 μl of oleic acid and 400 mg of $Cd(OAc)_2.2H_2O$. the resulting mix is the sonicated for 2 to 3h resulting in a white gel. Next, in a 50 mL three neck round bottom flask, a batch of CdSe NPLs in hexane was placed under argon flow to evaporated most of the hexane, the remaining part was then dissolved in 12 mL of ODE and 100 mg of $Cd(propionate)_2$ were added to the reaction mixture. It was then stirred under vacuum at 110°C for 20 min. After this degassing step, the mixture was placed under argon and heated to 235°C. Using a syringe pump, the CdS growth solution was added dropwise (3 mL/h) in time varying from 2 to 12 min depending on the desired CdS thickness.

The solution was then stirred at 235°C for another 5 min, and allowed to cool to room temperature. At 160 °C 2 mL of oleic acid where added. The solution was diluted in 20 mL of hexane and then centrifuged at 6000 rpm for 10 min. The supernatant was discarded and the precipitated NPLs were resuspended in hexane.

Synthesis of type-II CdSe/CdTe core/crown NPLs. First, 128 mg of elemental Te was dissolved in 1 mL of TOP (1M TOP-Te solution). The growth solution was prepared by mixing 75 μL of the 1M TOP-Te with 1mL of ODE right before injection. Next, in a 50 mL three neck round bottom flask, a batch of CdSe NPLs in hexane was placed under argon flow to evaporate most of the hexane, the remaining part was then dissolved in 12 mL of ODE and 100 mg of $Cd(propionate)_2$ were added to the reaction mixture. It was then stirred under vacuum at 110 °C for 20 min. After this degassing step, the mixture was placed under argon and heated to 235 °C. Using a syringe pump, the Te growth solution was added dropwise (3 mL/h). The addition was stopped when desired and the solution was stirred at 235 °C for another 5 min, and then cooled to room temperature. At 160 °C 2 mL of oleic acid where added. The solution was purified as described above.

Synthesis of CdSe/CdS/CdTe core/barrier/crown NPLs. For the preparation of the CdS and Te growth solutions, see previous sections. In a 50 mL three neck round bottom flask, a batch of CdSe in hexane was placed under argon flow to evaporated most of the hexane, the remaining part was then dissolved in 12 mL of ODE and 100 mg of $Cd(propionate)_2$ were added to the reaction mixture. It was then stirred under vacuum at 110 °C for 20 min. After this degassing step, the mixture was placed under argon and heated to 235 °C. Using a syringe pump, the CdS growth solution was added dropwise (3mL/h) in time varying from 1 to 12 min. Afterward, the solution was stirred at 235 °C for another 5 min. Using a syringe pump, the Te growth solution

was added dropwise (3 mL/h) in time varying from 2 to 16 min The solution was stirred at 235 °C for another 5 min, and then cooled to room temperature. At 160 °C, 2 mL of oleic acid were added. The solution purified as described above.

Transmission electron microscopy. A few drops of a dilute NPL suspension in hexane were dropped on a TEM grid (E. M. Sciences, Carbon film 300 mesh on copper) and inserted into a JEM 1011 electron microscope. Bright-field TEM images were recorded, and the length and width of typically 50/75 NPLs were analyzed. To prepare the specimen for STEM-EDS analysis, 3 uL of sample (Batch3) was drop casted onto ultrathin carbon/holey carbon coated Cu grid, and analyzed by an image-Cs-corrected JEOL JEM-2200FS TEM, with in-column filter (Ω-type) and Bruker XFlash 5060 SDD system. The presented elemental maps are unprocessed, *i.e.*, obtained simply by integration of the Kα peaks of S and Se and Lα peaks of Te and Cd.

Absorbance and time-resolved photoluminescence spectroscopy. A dilute NPL suspension in hexane was added to a 3 mL quartz cuvette. Absorbance spectra were measured with a Cary300 Varian spectrometer. Fluorescence spectra were recorded using a Edinburgh instruments FLS920 spectrofluorometer. Time-resolved fluorescence decay traces were recorded either with a pulsed LED (331 nm, CdSe/CdS core/crown reference samples, CdSe/CdS/CdTe Batch3), or a pulsed laser (405 nm, CdSe/CdTe core/crown reference samples, CdSe/CdS/CdTe Batch1, Batch2, Batch4). PL decay measurements were performed in time-correlated single photon mode, selecting a region of typically 10 nm around the peak maximum. The pulse period was set to be 1-2 us when monitoring the emission around 500 nm and 10-20 us when measuring the decay around 600 nm, to ensure complete decay between the pulses.

Single particle spectroscopy. Single particle PL measurements were performed on a home-built microscope setup. The excitation wavelength (400 nm) was generated by frequency doubling a 800 nm laser (MaiTai, 80 MHz, 100 fs). The repetition rate was reduced to 1 MHz by a pulse selector (Spectra Physics, Model 3980). The excitation was focused onto the NPLs using a microscope objective (50 X, NA = 0.80) and the photoluminescence from the NPLs was collected from the same objective. The pump fluence was around 20 $\mu J/cm^2$. The PL was recorded with an EMCCD (Prom EM HS, Princeton) camera attached to a spectrometer (Acton SP2300, Princeton). The sample was prepared by drop casting a dilute CBC solution onto precleaned glass cover slides.

Photoluminescence upconversion spectroscopy. A dilute solution of CBC nanocrystals dispersed in hexane was placed in 1×1 cm^2 quartz cuvette. The sample was excited by a 10 Hz, frequency tripled Nd:YAG Q-switched laser, pumping an optical parametric oscillator (Ekspla NT342/C/3/UVE), or by the residual laser pump at 1064 nm, all with a pulse duration of 5 ns. The laser excitation was focused on the sample and the fluorescence was collected in the orthogonal direction using a 20x NA 0.4 objective, spectrally filtered using an appropriate dielectric filter to block the excitation laser and a monochromator (Acton SpectraPro2150i) and measured by a photomultiplier (Hamamatsu R10699). The photomultiplier transient output was measured by a 600 MHz digital oscilloscope (LeCroy Wavesurfer 62Xs). The pulse energy was measured by a pyroelectric sensor (PE9-C, Ophir Optronics). Transient spectra were collected around the florescence peak for a series of different excitation powers and subtracted for dark noise. The spectrum was calculated by integrating the transient PMT counts using the respective decay peak boundaries. For the 1064 nm fundamental laser line, a 594 nm long pass dielectric filter and an RG615 color glass were used as clean up filters. The beam area was estimated using

a high resolution CCD camera (DCU223M, Thorlabs). The setup response function (RF) was measured to be 8 ns.

ASSOCIATED CONTENT

Supporting Information. Additional absorption, photoluminescence and TEM data. Theoretical modelling and additional fluorescence upconversion data. This material is available free of charge *via* the Internet at http://pubs.acs.org.

AUTHOR INFORMATION

Corresponding Authors

Iwan Moreels: iwan.moreels@ugent.be

Dan Oron: dan.oron@weizmann.ac.il

Juan I. Climente: climente@qfa.uji.es

Present Addresses

Guillaume H. V. Bertrand: CEA Saclay, 91191 Gif-sur-Yvette, France

Ayelet Teitelboim: The Molecular Foundry, Lawrence Berkeley National Laboratory, Berkeley, California 94720, United States

Author Contributions

The manuscript was written through contributions of all authors. All authors have given approval to the final version of the manuscript.

ACKNOWLEDGMENT

The present publication is realized with the support of the Ministero degli Affari Esteri e della Cooperazione Internazionale and the Ministry of Science, Technology and Space of the state of Israel (IONX-NC4SOL), and by the Crown Photonics Center of the Weizmann Institute of Science. This project has also received funding from the European Research Council (ERC) under the European Union's Horizon 2020 research and innovation programme (grant agreement No. 714876 PHOCONA). J. C and J. P. acknowledge the support from MINECO (project CTQ2017-83781-P) and UJI (project B2017-59). We also acknowledge the TEM facility of the Nematology Research Unit, member of the UGent TEM-Expertise center (life sciences).

REFERENCES

(1) Ghosh Chaudhuri, R.; Paria, S. Core/Shell Nanoparticles: Classes, Properties, Synthesis Mechanisms, Characterization, and Applications. *Chem. Rev.* **2012**, *112*, 2373–2433.
(2) Zhu, H.; Song, N.; Lian, T. Controlling Charge Separation and Recombination Rates in CdSe/ZnS Type I Core−Shell Quantum Dots by Shell Thicknesses. *J. Am. Chem. Soc.* **2010**, *132*, 15038–15045.
(3) Reiss, P.; Protière, M.; Li, L. Core/Shell Semiconductor Nanocrystals. *Small* **2009**, *5*, 154–168.
(4) Granados del Águila, A.; Groeneveld, E.; Maan, J. C.; de Mello Donegá, C.; Christianen, P. C. M. Effect of Electron–Hole Overlap and Exchange Interaction on Exciton Radiative Lifetimes of CdTe/CdSe Heteronanocrystals. *ACS Nano* **2016**, *10*, 4102–4110.
(5) Chen, O.; Zhao, J.; Chauhan, V. P.; Cui, J.; Wong, C.; Harris, D. K.; Wei, H.; Han, H.-S.; Fukumura, D.; Jain, R. K.; Bawendi, M. G. Compact High-Quality CdSe–CdS Core–Shell Nanocrystals with Narrow Emission Linewidths and Suppressed Blinking. *Nat. Mater.* **2013**, *12*, 445–451.
(6) García-Santamaría, F.; Chen, Y.; Vela, J.; Schaller, R. D.; Hollingsworth, J. A.; Klimov, V. I. Suppressed Auger Recombination in "Giant" Nanocrystals Boosts Optical Gain Performance. *Nano Lett.* **2009**, *9*, 3482–3488.

(7) Zhou, J.; Zhu, M.; Meng, R.; Qin, H.; Peng, X. Ideal CdSe/CdS Core/Shell Nanocrystals Enabled by Entropic Ligands and Their Core Size-, Shell Thickness-, and Ligand-Dependent Photoluminescence Properties. *J. Am. Chem. Soc.* **2017**, *139*, 16556–16567.
(8) Eshet, H.; Grünwald, M.; Rabani, E. The Electronic Structure of CdSe/CdS Core/Shell Seeded Nanorods: Type-I or Quasi-Type-II? *Nano Lett.* **2013**, *13*, 5880–5885.
(9) Christodoulou, S.; Rajadell, F.; Casu, A.; Vaccaro, G.; Grim, J. Q.; Genovese, A.; Manna, L.; Climente, J. I.; Meinardi, F.; Rainò, G.; Stöferle, T.; Mahrt, R. F.; Planelles, J.; Brovelli, S.; Moreels, I. Band Structure Engineering *via* Piezoelectric Fields in Strained Anisotropic CdSe/CdS Nanocrystals. *Nat. Commun.* **2015**, *6*, 7905.
(10) Tessier, M. D.; Spinicelli, P.; Dupont, D.; Patriarche, G.; Ithurria, S.; Dubertret, B. Efficient Exciton Concentrators Built from Colloidal Core/Crown CdSe/CdS Semiconductor Nanoplatelets. *Nano Lett.* **2014**, *14*, 207–213.
(11) Coropceanu, I.; Rossinelli, A.; Caram, J. R.; Freyria, F. S.; Bawendi, M. G. Slow-Injection Growth of Seeded CdSe/CdS Nanorods with Unity Fluorescence Quantum Yield and Complete Shell to Core Energy Transfer. *ACS Nano* **2016**, *10*, 3295–3301.
(12) Cassette, E.; Mahler, B.; Guigner, J.-M.; Patriarche, G.; Dubertret, B.; Pons, T. Colloidal CdSe/CdS Dot-In-Plate Nanocrystals with 2D-Polarized Emission. *ACS Nano* **2012**, *6*, 6741–6750.
(13) Pietryga, J. M.; Park, Y.-S.; Lim, J.; Fidler, A. F.; Bae, W. K.; Brovelli, S.; Klimov, V. I. Spectroscopic and Device Aspects of Nanocrystal Quantum Dots. *Chem. Rev.* **2016**, *116*, 10513–10622.
(14) Ithurria, S.; Tessier, M. D.; Mahler, B.; Lobo, R. P. S. M.; Dubertret, B.; Efros, A. L. Colloidal Nanoplatelets with Two-Dimensional Electronic Structure. *Nat. Mater.* **2011**, *10*, 936–941.
(15) Khan, A. H.; Brescia, R.; Polovitsyn, A.; Angeloni, I.; Martín-García, B.; Moreels, I. Near-Infrared Emitting Colloidal PbS Nanoplatelets: Lateral Size Control and Optical Spectroscopy. *Chem. Mater.* **2017**, *29*, 2883–2889.
(16) Christodoulou, S.; Climente, J. I.; Planelles, J.; Brescia, R.; Prato, M.; Martín-García, B.; Khan, A. H.; Moreels, I. Chloride-Induced Thickness Control in CdSe Nanoplatelets. *Nano Lett.* **2018**, *18*, 6248–6254.
(17) Naeem, A.; Masia, F.; Christodoulou, S.; Moreels, I.; Borri, P.; Langbein, W. Giant Exciton Oscillator Strength and Radiatively Limited Dephasing in Two-Dimensional Platelets. *Phys. Rev. B* **2015**, *91*, 121302.
(18) Scott, R.; Achtstein, A. W.; Prudnikau, A.; Antanovich, A.; Christodoulou, S.; Moreels, I.; Artemyev, M.; Woggon, U. Two Photon Absorption in II–VI Semiconductors: The Influence of Dimensionality and Size. *Nano Lett.* **2015**, *15*, 4985–4992.
(19) Rowland, C. E.; Fedin, I.; Zhang, H.; Gray, S. K.; Govorov, A. O.; Talapin, D. V.; Schaller, R. D. Picosecond Energy Transfer and Multiexciton Transfer Outpaces Auger Recombination in Binary CdSe Nanoplatelet Solids. *Nat. Mater.* **2015**, *14*, 484–489.
(20) Ithurria, S.; Talapin, D. V. Colloidal Atomic Layer Deposition (c-ALD) Using Self-Limiting Reactions at Nanocrystal Surface Coupled to Phase Transfer between Polar and Nonpolar Media. *J. Am. Chem. Soc.* **2012**, *134*, 18585–18590.
(21) Kelestemur, Y.; Guzelturk, B.; Erdem, O.; Olutas, M.; Gungor, K.; Demir, H. V. Platelet-In-Box Colloidal Quantum Wells: CdSe/CdS@CdS Core/Crown@Shell Heteronanoplatelets. *Adv. Funct. Mater.* **2016**, *26*, 3570–3579.

(22) Sun, H.; Buhro, W. E. Core–Shell Cadmium Telluride Quantum Platelets with Absorptions Spanning the Visible Spectrum. *ACS Nano* **2019**, *13*, 6982–6991.
(23) Altintas, Y.; Quliyeva, U.; Gungor, K.; Erdem, O.; Kelestemur, Y.; Mutlugun, E.; Kovalenko, M. V.; Demir, H. V. Highly Stable, Near-Unity Efficiency Atomically Flat Semiconductor Nanocrystals of CdSe/ZnS Hetero-Nanoplatelets Enabled by ZnS-Shell Hot-Injection Growth. *Small* **2019**, *15*, 1804854.
(24) Khan, A. H.; Pinchetti, V.; Tanghe, I.; Dang, Z.; Martín-García, B.; Hens, Z.; Van Thourhout, D.; Geiregat, P.; Brovelli, S.; Moreels, I. Tunable and Efficient Red to Near-Infrared Photoluminescence by Synergistic Exploitation of Core and Surface Silver Doping of CdSe Nanoplatelets. *Chem. Mater.* **2019**, *31*, 1450–1459.
(25) Polovitsyn, A.; Dang, Z.; Movilla, J. L.; Martín-García, B.; Khan, A. H.; Bertrand, G. H. V.; Brescia, R.; Moreels, I. Synthesis of Air-Stable CdSe/ZnS Core–Shell Nanoplatelets with Tunable Emission Wavelength. *Chem. Mater.* **2017**, *29*, 5671–5680.
(26) Lhuillier, E.; Pedetti, S.; Ithurria, S.; Nadal, B.; Heuclin, H.; Dubertret, B. Two-Dimensional Colloidal Metal Chalcogenides Semiconductors: Synthesis, Spectroscopy, and Applications. *Acc. Chem. Res.* **2015**, *48*, 22–30.
(27) Li, Q.; Wu, K.; Chen, J.; Chen, Z.; McBride, J. R.; Lian, T. Size-Independent Exciton Localization Efficiency in Colloidal CdSe/CdS Core/Crown Nanosheet Type-I Heterostructures. *ACS Nano* **2016**, *10*, 3843–3851.
(28) Pedetti, S.; Ithurria, S.; Heuclin, H.; Patriarche, G.; Dubertret, B. Type-II CdSe/CdTe Core/Crown Semiconductor Nanoplatelets. *J. Am. Chem. Soc.* **2014**, *136*, 16430–16438.
(29) Yadav, S.; Singh, A.; Sapra, S. Long-Lived Emission in Type-II CdS/ZnSe Core/Crown Nanoplatelet Heterostructures. *J. Phys. Chem. C* **2017**, *121*, 27241–27246.
(30) Dede, D.; Taghipour, N.; Quliyeva, U.; Sak, M.; Kelestemur, Y.; Gungor, K.; Demir, H. V. Highly Stable Multicrown Heterostructures of Type-II Nanoplatelets for Ultralow Threshold Optical Gain. *Chem. Mater.* **2019**, *31*, 1818–1826.
(31) Kelestemur, Y.; Guzelturk, B.; Erdem, O.; Olutas, M.; Erdem, T.; Usanmaz, C. F.; Gungor, K.; Demir, H. V. CdSe/CdSe1–xTex Core/Crown Heteronanoplatelets: Tuning the Excitonic Properties without Changing the Thickness. *J. Phys. Chem. C* **2017**, *121*, 4650–4658.
(32) Dufour, M.; Steinmetz, V.; Izquierdo, E.; Pons, T.; Lequeux, N.; Lhuillier, E.; Legrand, L.; Chamarro, M.; Barisien, T.; Ithurria, S. Engineering Bicolor Emission in 2D Core/Crown CdSe/CdSe1–XTex Nanoplatelet Heterostructures Using Band-Offset Tuning. *J. Phys. Chem. C* **2017**, *121*, 24816–24823.
(33) Liu, B.; Delikanli, S.; Gao, Y.; Dede, D.; Gungor, K.; Demir, H. V. Nanocrystal Light-Emitting Diodes Based on Type II Nanoplatelets. *Nano Energy* **2018**, *47*, 115–122.
(34) Galland, C.; Brovelli, S.; Bae, W. K.; Padilha, L. A.; Meinardi, F.; Klimov, V. I. Dynamic Hole Blockade Yields Two-Color Quantum and Classical Light from Dot-In-Bulk Nanocrystals. *Nano Lett.* **2013**, *13*, 321–328.
(35) Deutsch, Z.; Schwartz, O.; Tenne, R.; Popovitz-Biro, R.; Oron, D. Two-Color Antibunching from Band-Gap Engineered Colloidal Semiconductor Nanocrystals. *Nano Lett.* **2012**, *12*, 2948–2952.
(36) Soni, U.; Pal, A.; Singh, S.; Mittal, M.; Yadav, S.; Elangovan, R.; Sapra, S. Simultaneous Type-I/Type-II Emission from CdSe/CdS/ZnSe Nano-Heterostructures. *ACS Nano* **2014**, *8*, 113–123.

(37) V. Bertrand, G. H.; Polovitsyn, A.; Christodoulou, S.; Hossain Khan, A.; Moreels, I. Shape Control of Zincblende CdSe Nanoplatelets. *Chem. Commun.* **2016**, *52*, 11975–11978.
(38) Tenne, R.; Pedetti, S.; Kazes, M.; Ithurria, S.; Houben, L.; Nadal, B.; Oron, D.; Dubertret, B. From Dilute Isovalent Substitution to Alloying in CdSeTe Nanoplatelets. *Phys. Chem. Chem. Phys.* **2016**, *18*, 15295–15303.
(39) Wei, S.-H.; Zhang, S. B.; Zunger, A. First-Principles Calculation of Band Offsets, Optical Bowings, and Defects in CdS, CdSe, CdTe, and Their Alloys. *J. Appl. Phys.* **2000**, *87*, 1304–1311.
(40) V.F. Gantmakher; Y.B. Levinson; *Carrier Scattering in Metals and Semiconductors*, 1st Ed.; North Holland Physics Publishing: Amsterdam, 1987; Vol. 19.
(41) Wu, M.; Congreve, D. N.; Wilson, M. W. B.; Jean, J.; Geva, N.; Welborn, M.; Van Voorhis, T.; Bulović, V.; Bawendi, M. G.; Baldo, M. A. Solid-State Infrared-To-Visible Upconversion Sensitized by Colloidal Nanocrystals. *Nat. Photon.* **2016**, *10*, 31–34.
(42) Wen, S.; Zhou, J.; Zheng, K.; Bednarkiewicz, A.; Liu, X.; Jin, D. Advances in Highly Doped Upconversion Nanoparticles. *Nat. Commun.* **2018**, *9*, 1–12.
(43) Zheng, W.; Huang, P.; Gong, Z.; Tu, D.; Xu, J.; Zou, Q.; Li, R.; You, W.; Bünzli, J.-C. G.; Chen, X. Near-Infrared-Triggered Photon Upconversion Tuning in All-Inorganic Cesium Lead Halide Perovskite Quantum Dots. *Nat. Commun.* **2018**, *9*, 1–9.
(44) Deutsch, Z.; Neeman, L.; Oron, D. Luminescence Upconversion in Colloidal Double Quantum Dots. *Nat. Nanotechnol.* **2013**, *8*, 649–653.
(45) Teitelboim, A.; Oron, D. Broadband Near-Infrared to Visible Upconversion in Quantum Dot–Quantum Well Heterostructures. *ACS Nano* **2016**, *10*, 446–452.
(46) Yang, G.; Meir, N.; Raanan, D.; Oron, D. Band Gap Engineering Improves the Efficiency of Double Quantum Dot Upconversion Nanocrystals. *Adv. Funct. Mater.* **2019**, *29*, 1900755.
(47) Kwon, S. J.; Lee, G. Y.; Jung, K.; Jang, H. S.; Park, J.-S.; Ju, H.; Han, I. K.; Ko, H. A Plasmonic Platform with Disordered Array of Metal Nanoparticles for Three-Order Enhanced Upconversion Luminescence and Highly Sensitive Near-Infrared Photodetector. *Adv. Mater.* **2016**, *28*, 7899–7909.
(48) Zhou, B.; Shi, B.; Jin, D.; Liu, X. Controlling Upconversion Nanocrystals for Emerging Applications. *Nat. Nanotechnol.* **2015**, *10*, 924–936.
(49) Wilhelm, S. Perspectives for Upconverting Nanoparticles. *ACS Nano* **2017**, *11*, 10644–10653.

TOC GRAPHIC AND SYNOPSIS

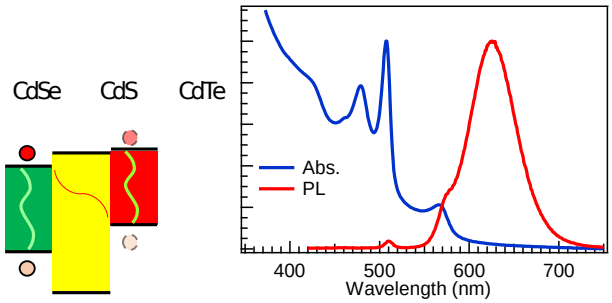
CdSe
CdS
CdTe
Abs.
PL
400
500
600
700
Wavelength (nm)

CdSe/CdS/CdTe Core/Barrier/Crown Nanoplatelets: Synthesis, Optoelectronic Properties and Multi-Photon Fluorescence Upconversion - Supporting Information

Ali Hossain Khan,[1,2] Guillaume H. V. Bertrand,[2] Ayelet Teitelboim,[3] Chandra Sekhar M.,[1] Anatolii Polovitsyn,[2] Rosaria Brescia,[2] Josep Planelles,[4] Juan Ignacio Climente,[4,] Dan Oron,[3,*] and Iwan Moreels[1,2,*]*

[1] Department of Chemistry, Ghent University, Krijgslaan 281-S3, 9000 Ghent, Belgium.

[2] Istituto Italiano di Tecnologia, Via Morego 30, 16163 Genova, Italy.

[3] Department of Physics of Complex Systems, Weizmann Institute of Science, Rehovot 7610001, Israel.

[4] Departament de Química Física i Analítica, Universitat Jaume I, 12080 Castelló de la Plana, Spain.

Present Addresses

Guillaume H. V. Bertrand: CEA Saclay, 91191 Gif-sur-Yvette, France

Ayelet Teitelboim: The Molecular Foundry, Lawrence Berkeley National Laboratory, Berkeley, California 94720, United States

1. ADDITIONAL ABSORPTION, PHOTOLUMINESCENCE AND TEM DATA

a

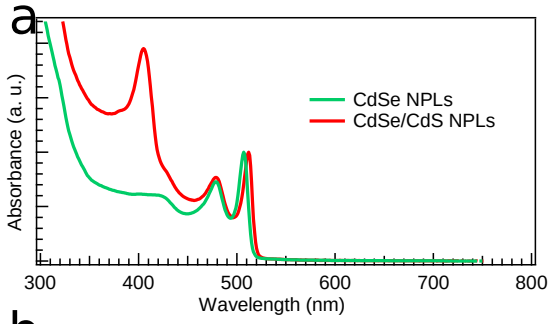

b

c

d

Sample name	Abs_{max} (nm)	PL_{max} (nm)	τ_{av} (ns)
CdSe NPLs	507	510	8.2
CdSe/CdS NPLs	511	513	3.3

Figure S1. (a) Absorption spectra, (b) PL spectra and (c) PL decay traces of CdSe core (green) and CdSe/CdS core/crown (red) NPLs. For the latter, samples were excited at 331 nm with a pulsed LED. (d) Table containing the value of absorption and PL peak maximum and the amplitude-weighted average lifetime of CdSe core and CdSe/CdS core/crown NPLs.

a

b

c

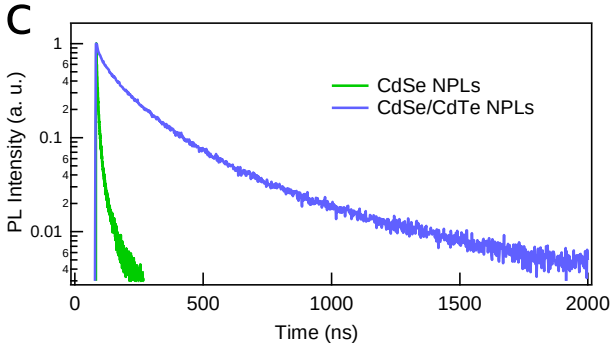

d

Sample name	PL_{max} (nm)	τ_{av} (ns)
CdSe NPLs	513	6.2
CdSe/CdTe NPLs	637	124

Figure S2. (a) Absorption spectra, (b) PL spectra and (c) PL decay traces of CdSe core and CdSe/CdTe core/crown NPLs. For the latter, samples were excited at 405 nm. (d) Table containing the value of absorption and PL peak maximum and the amplitude-weighted average lifetime of CdSe core and CdSe/CdTe core/crown NPLs.

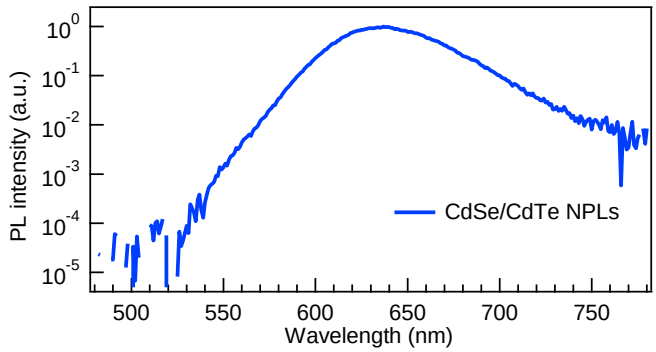

Fit name	Emission of	Peak location (nm)	FWHM (nm)	Area %
Peak 1	CdSe	514	7.0	0.001
Peak 2	type-II	637	59.7	99.996

Figure S3. PL spectrum of CdSe/CdTe core/crown NPLs. The emission from the CdSe direct transition is negligible. The table is the summary of the peak fitting results.

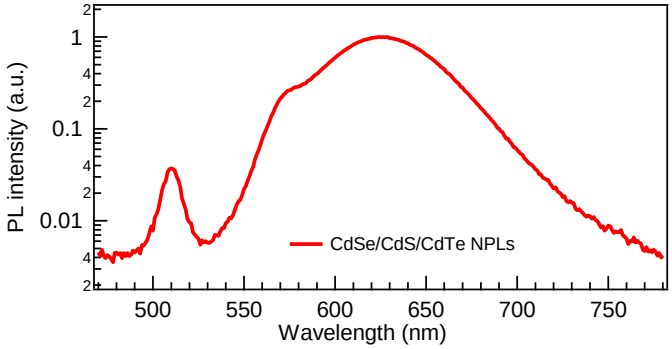

	Emission	Peak location (nm)	FWHM (nm)	Area (%)
Peak 1	CdSe	510	11.1	0.5
Peak 2	CdTe	574	21.0	4.2
Peak 3	type-II	625	58.8	95.3

Figure S4. PL spectrum of CdSe/CdS/CdTe CBC NPLs. In contrast with CdSe/CdTe NPLs, clear features for the CdSe and CdTe direct transitions are observed. The table is the summary of the peak fitting results.

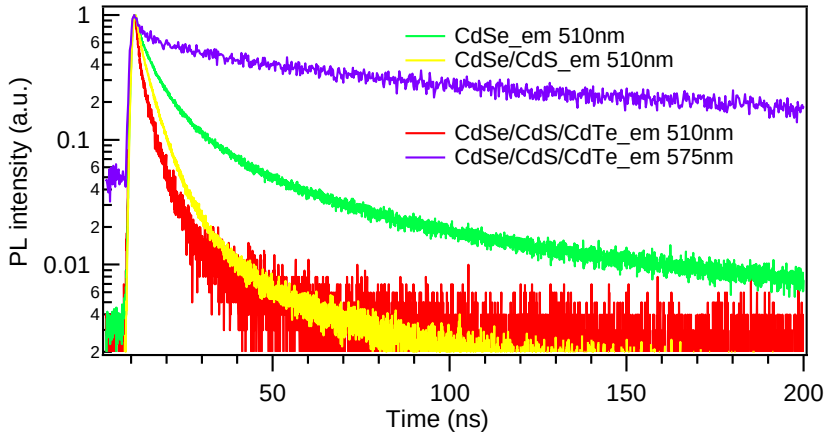

Name	A_1	τ_1	A_2	τ_2	A_3	τ_3	τ_{av} (ns)
CdSe@510	0.32	1.4	0.57	6.3	0.13	33.6	8.2
CB@510	0.43	1.6	0.59	4.6	0.03	25.1	3.9
CBC@510	0.70	1.2	0.37	4.4	0.01	30.1	2.6
CBC@575	0.38	2.9	0.31	39.4	0.26	225.2	76
CBC@625	0.24	15.6	0.47	122	0.22	481	182

Figure S5. Upper panel: PL decay traces of CdSe core (green) CdSe/CdS (yellow), and CBC (red and purple) NPLs (Batch3) at different emission wavelength. Lower panel: Table containing the decay amplitudes and lifetimes, and the amplitude-weighted average lifetime of the different NPLs.

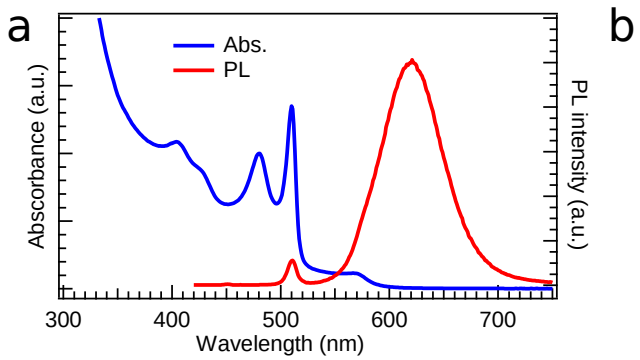

Figure S6. (a) Absorption and PL of the CBC NPLs with wider CdS barrier (Batch5). (b) PLE spectra of CBC NPLs at different emission wavelengths.

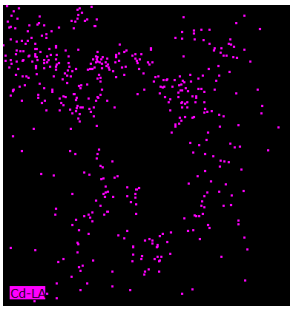

Figure S7. HAADF-STEM images (leftmost and rightmost) of CBC NPLs (Batch3) showing the degradation of the NPL structure after 19 minutes of acquisition of STEM-EDS elemental maps (using a 1 nm spot size). The acquired elemental maps for Cd, S, Se and Te are shown in the central panels.

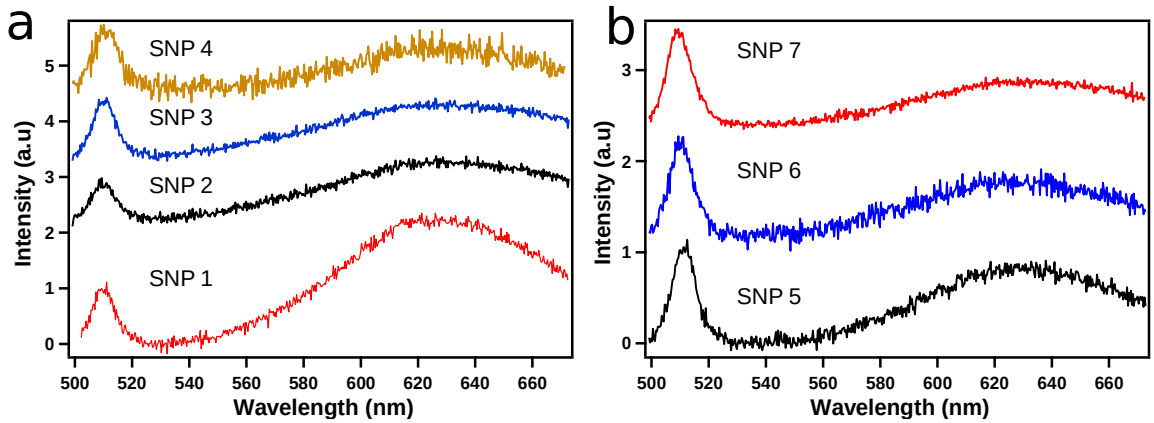

Figure S8. (a-b) PL spectra of various single CBC NPLs, showing the presence of both CdSe and type-II emission. For single particle PL measurement batch 5 CBC NPLs have been used, which had PL quantum efficiency of 15%.

Table S1: The peak position and FWHM of CdSe and type II emission of various single NPLs and corresponding close-packed thin film.

CdSe/CdS/CdTe (CBC) NPLs	Type I		Type II	
	Peak Maximum (nm)	FWHM (nm)	Peak Maximum (nm)	FWHM (nm)
Film	511.9	13.6	631.4	81.7
SNP 1	510.0	10.8	629.9	88.2
SNP 2	509.9	10.9	632.8	106.1
SNP 3	510.3	10.2	632.2	109.6
SNP 4	510.9	10.7	629.2	74.8
SNP 5	511.5	10.6	631.3	80.6
SNP 6	510.4	10.9	629.5	87.4
SNP 7	509.8	11.2	633.8	90.3

Table S2. The dimensions (obtained from TEM) of CdS barrier and CdTe crown achieved by injecting different amounts of Cd/S and Te growth solutions. The injection rate of the precursor solution was always kept at a fixed rate of 3 mL per hour. For some samples, negative values were be obtained when initial and final particle dimensions were similar, indicating a negligible CdS barrier and/or CdTe crown growth.

	Core	**Core/Barrier**		**Core/Barrier/Crown**	
Name	Length × Width (nm x nm)	CdS solution injection rate (min)	CdS Barrier length × width (nm x nm)	Te solution injection rate (min)	CdTe crown length × width (nm x nm)
Batch1	31.1 x 6.4	2 min	-0.05 × 0.4	1 min	0.8 × -0.1
Batch2	30.3 x 6.4	4 min	0.6 × 1.1	4 min	2.5 × 0.4
Batch3	35.6 x 4.2	2 min	0.9 × 0.7	3 min	7.1 × 1.8
Batch4	24.3 x 5.0	12 min	8.8 × 2.3	16 min	7.5 × 2.9
Batch5	40.5 × 5.1	3 min	2.0 × 0.8	2 min	2.6 × 0.8

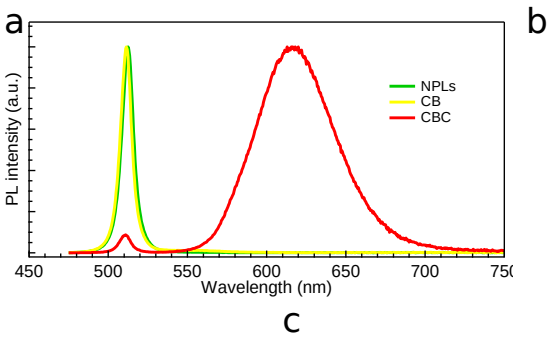

	Area CdSe (%)	Area CdTe (%)	Area type-II (%)
Batch1	1.3	0.8	97.8
Batch2	0.5	6.7	92.8
Batch4	1.8	2.8	95.4

Figure S9. PL spectra for core, core/barrier and core/barrier/crown samples of (a) Batch1 (narrow barrier), (b) Batch2 (medium barrier) and (c) Batch4 (wide barrier, bottom). Next to the indirect transitions, two additional features are observed that can be assigned to CdSe and CdTe emission. Relative weights are reported in the table. PL spectra of Batch3 are presented in Figure S4 and Figure 2 of the main text.

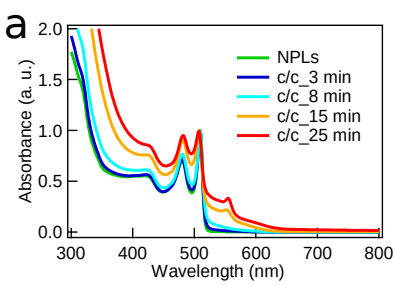

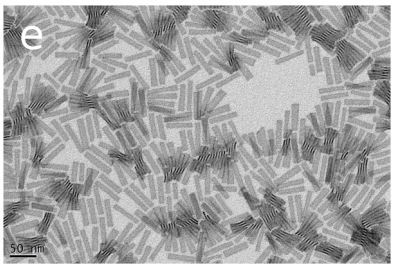

f

Sample Name	Length î Width (nm^2)	PL_{max} (nm)	τ_{av} (ns)
CdSe Core	37.5 x 5.5	513	6.7
c/c_3min	39.2 x 6.4	614	104.7
c/c_8min	40.8 x 7.0	625	53.7
c/c_15min	43.7 x 8.1	637	131.7
c/c_25min	49.2 x 9.5	646	220.7

Figure S10. (a) Absorption spectra, (b) PL spectra and (c) PL decay traces of CdSe core and different CdSe/CdTe core/crown NPLs respectively. TEM images of (d) CdSe core and (e) CdSe/CdTe core/crown (sample c/c_25 min) NPLs. (f) Table containing the dimensions, value of PL peak maximum and the amplitude-weighted average lifetime of CdSe core and different CdSe/CdTe core/crown NPLs.

Table S3. Table with the PL peak position and amplitude-weighted average lifetime of the core, core/barrier and core/barrier/crown NPLs.

	core		**core/barrier**		**core/barrier/crown**		
	PL_core	τ_core	PL_core	τ_core	PL_core	PL_typeII	τ_typeII
Batch1	512	5.5	511	5.0	511	617	160
Batch2	512	5.8	513	4.2	513	621	157
Batch3	510	8.2	510	3.9	510	625	182
Batch4	509	4.0	513	2.7	513	642	182

2. THEORETICAL MODELING

Purpose and Method

To better understand the opto-electronic properties of CdSe/CdS/CdTe CBC NPLs, we carried out numerical simulations of the conduction band electrons and valence band (heavy) holes.

In view of the picture sketched in the main text, hole states are calculated using the Hamiltonian:

$$H_h = \frac{1}{2}\hat{p}\frac{1}{m_h(\vec{r})}\hat{p} + V_{self}^{\square} + V_{bo}^{h} + V_{strain}^{h} .$$

Here m_h is the (position dependent) hole effective mass, p the three-dimensional momentum operator, V_{self} the self-energy potential arising from the dielectric mismatch between the inorganic NPL and the organic surroundings –which we calculate taking analytical quantum well expressions[1], $V_{bo}{}^{h}$ is the (squared-well) valence band offset potential and $V_{strain}{}^{h}$ the deformation potential strain Hamiltonian:

$$V_{strain}^{h} = \left(a_v + \frac{b}{2}\right)\left(\epsilon_{xx} + \epsilon_{yy}\right) + \left(a_v - b\right)\epsilon_{zz},$$

with a_v and b the valence band deformation potentials, and ϵ_{ij} a strain tensor component.

For the electron, the full Hamiltonian reads:

$$H_e = \frac{1}{2}\hat{p}\frac{1}{m_e(\vec{r})}\hat{p} + V_{self}^{\square} + V_{bo}^{e} + V_{strain}^{e} + V_{coul}^{e},$$

where m_e is the electron effective mass, $V_{bo}{}^{e}$ is the conduction band offset potential, $V_{strain}{}^{e}$ the deformation potential strain Hamiltonian:

$$V_{strain}^{e} = a_c\left(\epsilon_{xx} + \epsilon_{yy} + \epsilon_{zz}\right),$$

with a_c the conduction band deformation potential, and $V_{coul}{}^{e}$ the Coulomb attraction exerted by the hole ground state (localized in the CdTe crown) on the electron, which includes the enhancement due to the low dielectric constant of the NPL surroundings.

Strain maps are calculated in the continuous medium model by minimizing the elastic energy. The boundary conditions are zero normal stress for the free surface. The Coulomb potential is obtained by solving Poisson's equation with the hole ground state as the source electric charge. Strain tensor elements, Coulomb electrostatic potential and eigenfunctions of H_e and H_h are obtained using Comsol 4.2 software. The calculations are simplified by imposing D_{2h} symmetry planes to the rectangular NPL, which allows us to identify electron and hole eigenstates by their point group symmetry. Thus, we label states as $|\Gamma, n\rangle$, which is the n-th state of the Γ irreducible representation. Material parameters used for the calculations are summarized in **Table S3**. Also, band offsets between bulk semiconductor materials are given in **Figure 4** of the main text.

Table S4. Summary of material parameters used in the calculation. m_0 is the free electron mass. The relative dielectric constant outside the NPL is 2 and the electron (hole) band offset with the organic medium 2.5 eV from the bottom (top) of the conduction (valence) band of CdSe. Band offsets are taken from Ref. 2, deformation potentials a_c and a_v are taken from Ref. 3, relative dielectric constant are approximate values between static and high-frequency dielectric constants, CdSe hole masses are taken from Ref. 4, and the rest of parameters from Ref. 5.

Parameter	**CdSe**	**CdS**	**CdTe**	**Parameter**	**CdSe**	**CdS**	**CdTe**
m_e^z (m_0)	0.11	0.14	0.09	m_h^z (m_0)	1.14	0.39	0.53
m_e^{xy} (m_0)	0.11	0.14	0.09	m_h^{xy} (m_0)	0.38	0.20	0.14
a_c (eV)	-2.00	-2.54	-2.81	a_v / b (eV)	0.9/-0.8	0.4/-1.05	0.89/-1.0
$C11$ (GPa)	66.7	77	53.5	ε_r	10	10	10
$C12$ (GPa)	46.3	53.9	36.9	a (Å)	6.077	5.825	6.481
$C44$ (GPa)	22.3	23.6	20.2				

Results and Discussion

We first analyzed the influence of the CdS barrier on the elastic strain. CdS has a strong lattice mismatch (over 10%) with CdTe, which is expected to alter the CdS/CdTe interface. **Figure S11** shows the hydrostatic strain in the wide (a) and narrow (b) barrier CBC NPLs (same as in **Figure 4** of the main text). As can be seen, most of the strain concentrates on the CdS barrier and –especially- on the first nm around the CdS/CdTe interface. By contrast, the center of the CdSe core and the outer part of the CdTe crown are only weakly affected.

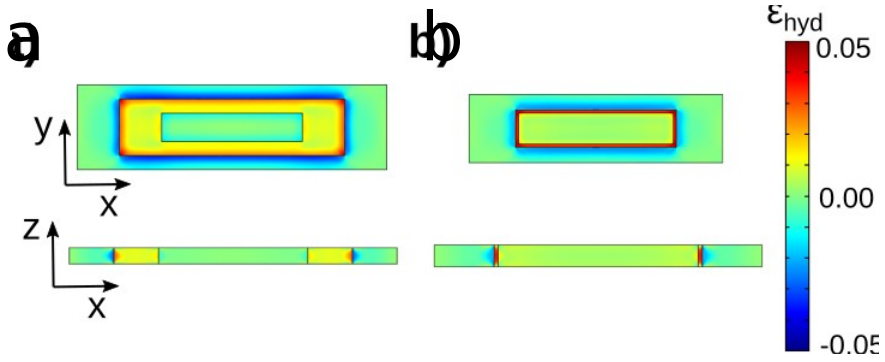

Figure S11. Hydrostatic strain $(\epsilon_{xx}+\epsilon_{yy}+\epsilon_{zz})$ in (a) wide and (b) narrow CdS barrier NPLs. The top (bottom) panels show an in-plane (vertical) section of the NPLs. Positive and negative strain are tensile and compressive, respectively.

The strain is tensile on the CdS side and compressive on the CdTe one. Considering the sign of the deformation potentials (**Table S4**), this means that a strain-induced potential well (barrier) forms on the CdS (CdTe) side of the barrier-crown interface, as seen in **Figure 4i-4j** of the main text.

The band profile of a typical wide barrier CBC NPL is shown in **Figure S12**. The figure completes the data of **Figure 4f-4j** of the main text for the wide CdS barrier NPL. Left and right columns show the potential corresponding to valence band (left) and conduction band (right). The top graphs are a 2D map of the potential on the (*x*,*y*) plane at mid-height. The central panels are 1D profiles along the *x*- semi-axis (as in **Figure 4f-4j**) and the bottom ones along the *y*- semi-axis. The role of band-offset and strain described in the main text holds all over the NPL plane. The Coulomb potential that the hole exerts on the electron (blue line) is more attractive at the CdS/CdTe interface along the *x*-axis than at the interface along the *y*-axis (cf. **Figure S12e-S12f**). This is because the narrow CdTe crown in the *y*-direction prevents a buildup of significant charge density in that region. The self-energy potential provides a constant shift all over the structure, which does not modify the relative band alignment.

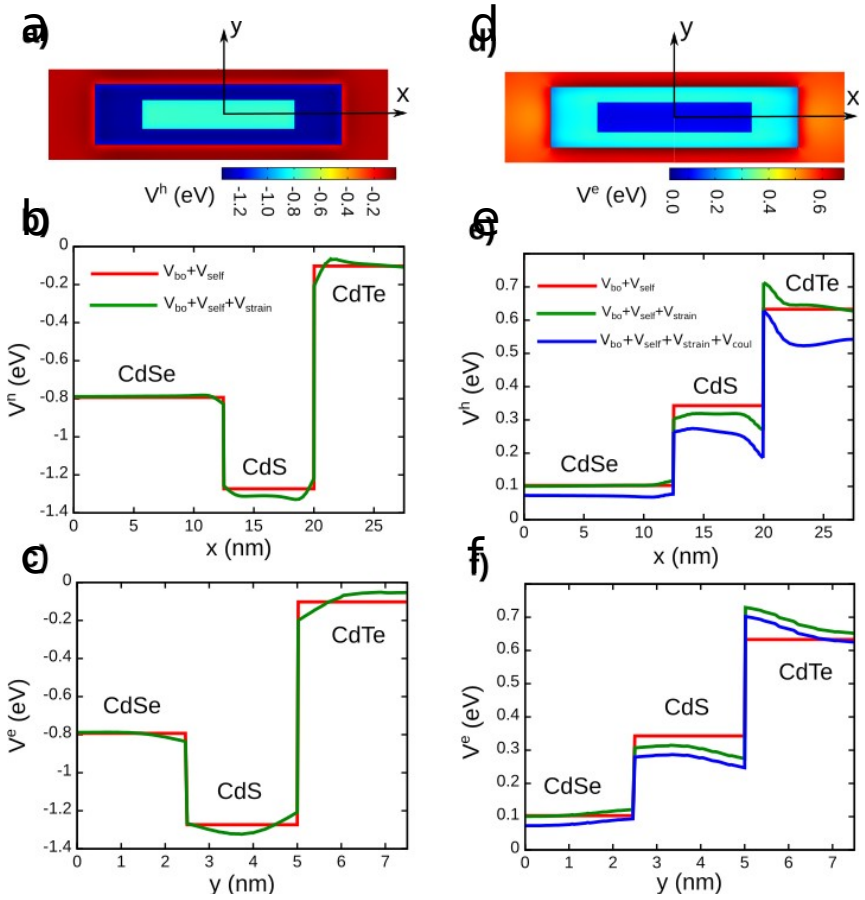

Figure S12. Potential landscape seen by a valence band hole (left) and a conduction band electron (right) in wide-barrier CBC NPLs. Top panels show a 2D in-plane cross-section (for *z* in the center of the NPL), while mid and bottom panels show the 1D profile along *x*- and *y*-semi-axes. In the 1D plots, red and green lines show the potential excluding and including the influence of strain, respectively. For electrons, we add Coulomb interaction with the hole ground state (blue line) to obtain the highest possible barrier at the CdS/CdTe interface.

The band structure shown in **Figure S12** gives rise to preferential localization of electron and –especially– hole states either in the core or in the crown, as discussed in **Figure 5** of the main text. This can be expected to affect the intraband transition rates from crown to core states, facilitating the formation of meta-stable states. The precise value of transition rates depends on the nature of the process (phononic, photonic, Auger, etc), however, quantitative calculations are beyond the scope of this paper. Assuming phonon decay is involved, as is often the case in colloidal quantum dots, the high surface-to-volume ratio of NPLs implies that confined, surface and interface phonon modes are expected to play a role.[6,7] These are not well described in continuum models like $k \cdot p$ theory. In any case, every scattering mechanism involves coupling the initial and final electronic states. If these are spatially separated, the scattering becomes less efficient.

For illustration purposes, we calculated transition dipole matrix elements, which are relevant to both photonic and phononic intraband processes. We considered that the lowest energy electron or hole states are *s*-like, *i.e.* they form a basis of the A_g irreducible representation in the D_{2h} group. In turn, *x*-, *y*- and *z*-coordinate operators form the basis of the B_{3u}, B_{2u} and B_{1u} irreducible representations. Then, the selection rule implies that the final state *f* should have B_{3u}, B_{2u} and B_{1u} symmetry, for *x*-, *y*- and *z*-components of the photon/phonon wave expansion. The largest dipole moments are expected along the *x*-direction (the long axis of the NPL). Then, we compute matrix elements of the kind $\langle B_{3u}, n' | x | A_g, n \rangle$ to evaluate ¿$\langle f | \vec{r} | i \rangle$∨¿.

We considered as the initial state *i* the lowest hole (electron) state localized in CdSe (CdTe), and then computed the matrix element to all lower-energy states, to see if the respective CdSe-localized hole or CdTe-localized electron state has limited overlap with lower-lying states and is thus long-lived. The results are summarized in **Figure S13**. Panels (a) and (b) show the dipole matrix elements for hole transitions from the CdSe-localized state to all lower energy states, which are mainly localized in CdTe. One can see the matrix element is orders of magnitude smaller in wide-barrier NPLs (panel (a)) than in narrow ones (panel (b)). This is because the strong localization either in the core or in the crown makes the overlap between initial and final states negligible. This finding supports the formation of meta-stable hole states in the core, especially in samples with a wide barrier, which may recombine with electrons radiatively before non-radiative relaxation takes place.

Panels (c) and (d) show the matrix elements for electron transitions from the CdTe crown to CdSe core localized states. One can notice that the dipole moment is much larger than in the case of holes. This is because electrons show partial localization on both sides of the CdS barrier, which implies that relaxation of electrons should be much faster than for holes. The thickness of the barrier does make a large difference in the average rates. However, in

accordance with experimental observations, narrowing the crown width (panels (e) and (f)) does provide an additional suppression of the dipole matrix elements. This is a consequence of the reduced electron localization on the short sides of the NPL, as mentioned in the discussion of **Figure 5** in the main text.

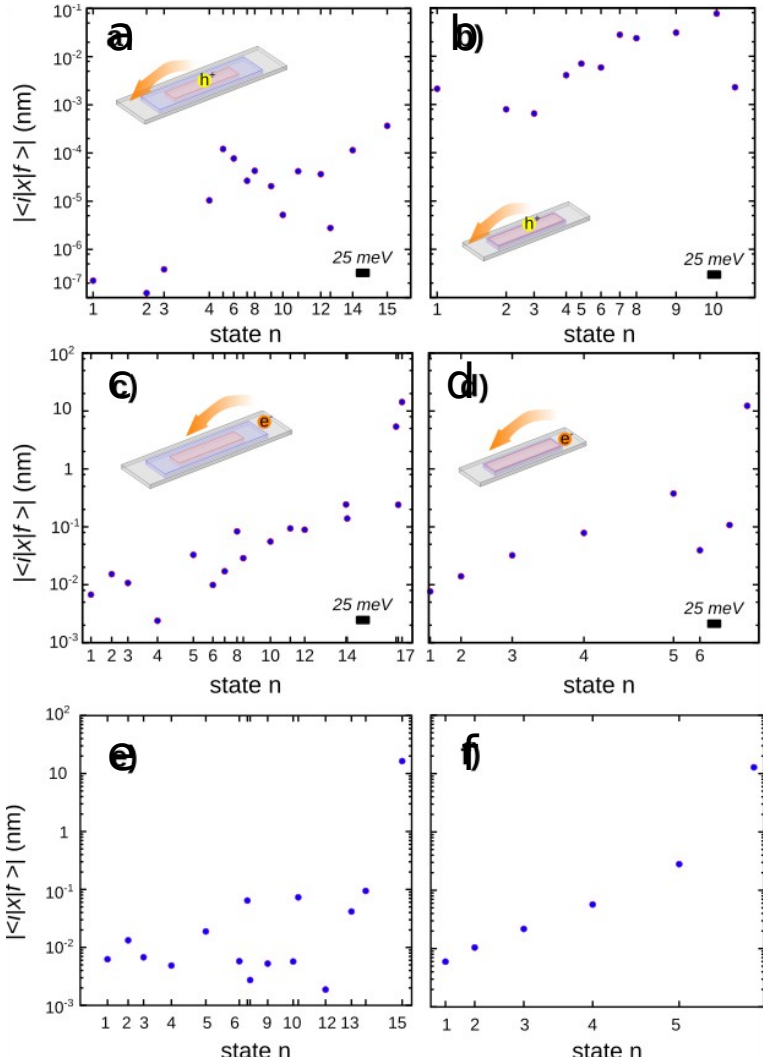

Figure S13. Logarithmic plot of dipole matrix element between: (a-b) the lowest hole state localized in the CdSe core, and all states below, (c-d) the lowest electron state localized in the CdTe crown, and all states below, (e-f) same as c-d but with narrow CdTe crown. Left and right columns refer to wide and narrow CdS barrier CBC NPLs. The structures are the same as in **Figure 5** of the main text.

3. ADDITIONAL FLUORESCENCE UPCONVERSION DATA

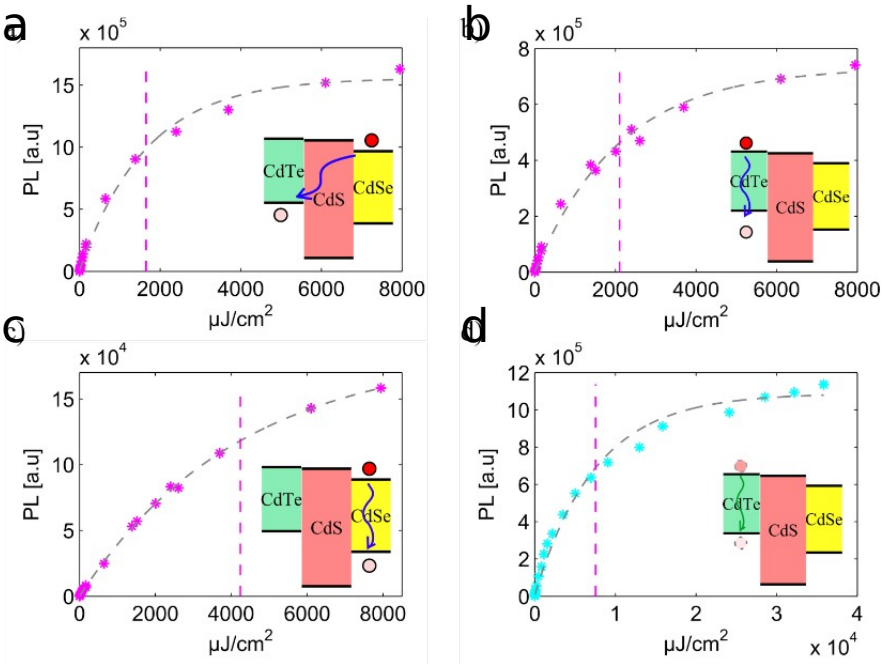

Figure S14. NPL linear saturation curves. (a-c) Linear saturation using 460 nm excitation monitored at 620, 580, 515 nm which corresponds to the indirect transition, the CdTe crown, and the CdSe core. Saturation intensities are equals to $I_{sat_{620}}^{ex_{460}} = 1.65 \frac{mJ}{cm^2}$, $I_{sat_{580}}^{ex_{460}} = 2.1 \frac{mJ}{cm^2}$, $I_{sat_{515}}^{ex_{460}} = 4.2 \frac{mJ}{cm^2}$, and are plotted as dashed vertical lines. (d) Linear saturation curve of the indirect transition using 580 nm excitation, exciting the CdTe crown and the indirect transition monitored at 620 nm. $I_{sat_{620}}^{ex_{580}} = 7.6 \frac{mJ}{cm^2}$ and is plotted as dashed vertical line.

4. REFERENCES

1. Kumagai, M.; Takagahara, T. Excitonic and Nonlinear-Optical Properties of Dielectric Quantum Well Structures. *Phys. Rev. B.* **1989**, *40*, 12359.
2. Li, Y.-H.; Walsh, A.; Chen, S.; Yin, W.-J.; Yang, J.-H.; Li, J.; Da Silva, J. L.; Gong, X. G.; Wei, S.-H. Revised *Ab Initio* Natural Band Offsets of All Group IV, II-VI, and III-V Semiconductors. *Appl. Phys. Lett.* **2009,** *94*, 212109.
3. Li, Y.-H.; Gong, X. G.; Wei, S.-H. *Ab Initio* All-Electron Calculation of Absolute Volume Deformation Potentials of IV-IV, III-V, and II-VI Semiconductors: The Chemical Trends *Phys. Rev. B* **2006,** *73*, 245206.
4. Norris, D. J.; Bawendi, M. G. Measurement and Assignment of the Size-Dependent Optical Spectrum in CdSe Quantum Dots *Phys. Rev. B* **1996,** *53*, 16338.
5. Adachi, S; *Handbook of Physical Properties of Semiconductors*, 1st Ed.; Kluwer Academic Publishers: Boston, **2004**; Vol. 3.
6. Scott, R.; Prudnikau, A. V.; Antanovich, A.; Christodoulou, S.; Riedl, T.; Bertrand, G. H.; Owschimikow, N.; Lindner, J. K.; Hens, Z.; Moreels, I.; Artemyev, M.; Woggon, U.; Achtstein, A. W. A Comparative Study Demonstrates Strong Size Tunability of Carrier–Phonon Coupling in CdSe-Based 2D and 0D Nanocrystals. *Nanoscale* **2019,** *11*, 3958-3967.
7. Pandya, R.: Chen, R. Y.; Cheminal, A.; Dufour, M.; Richter, J. M.; Thomas, T. H.; Ahmed, S.; Sadhanala, A.; Booker, E. P.; Divitini, G.; Deschler, F.; Greenham, N. C.; Ithurria, S.; A. Rao, Exciton–Phonon Interactions Govern Charge-Transfer-State Dynamics in CdSe/CdTe Two-Dimensional Colloidal Heterostructures. *J. Am. Chem. Soc.* **2018**, *140*, 14097-14111.